AREA AND VOLUME CHANGES OF ADAMS ICEFIELD FROM 1948 TO 2019, AXEL HEIBERG ISLAND, NUNAVUT, CANADA

by

Braden William Smeda

Supervisors:

Dr. Luke Copland, University of Ottawa

Dr. Laura Thomson, Queen's University

University of Ottawa

Ottawa, Ontario, Canada

December 2020

Abstract

There has been a marked increase in melt season length over the past two decades on glaciers and ice caps within Canada's Queen Elizabeth Islands (QEI). Prior to the year ~2000 land ice was in a state of slightly negative mass balance (-11 ± 11.5 Gt yr^{-1} over 1958-1995), but recent GRACE measurements suggest that mass losses averaged -33 ± 5 Gt yr^{-1} between 2003-2015. These losses have primarily been attributed to meltwater runoff, making the QEI one of the largest recent contributors to sea level rise outside of the ice sheets. Despite these losses, there is a lack of information concerning how a warming climate is affecting small (<1 km^2) ice bodies, which are considered sensitive indicators of change due to their short response time.

In this study, historical and contemporary aerial photographs, high resolution optical satellite imagery, and ground penetrating radar (GPR) surveys are used to determine area, thickness, mass and volume changes of Adams Icefield within Expedition Fiord, Axel Heiberg Island, Nunavut, over the past seven decades (1948/59-2019). Area changes are determined from a comparison of air photos acquired in 1948/59 with satellite images acquired since 1979. Contemporary (2001, 2012, 2019) digital elevation models (DEMs) were either collected or created from stereo satellite images, and via aerial photo surveys using Structure from Motion photogrammetry. DEM of Difference maps calculated from these DEMs provide volume and mass changes. Results illustrate a steady reduction in glacier area, thickness, and volume prior to the year ~2000, followed by a rapid increase in losses over the past two decades. As a result, Adams Icefield is now rapidly declining and is likely to completely disappear early in the twenty-second century.

Acknowledgements

Support for this research has been provided by the University of Ottawa, Queen's University, the Northern Scientific Training Program, ArcticNet, NSERC, and the Polar Continental Shelf Program. Support for travel to conferences and attendance of courses was generously provided by ArcticNet and RemoteEx.

I would first like to express my sincere appreciation to both my supervisors: Dr. Luke Copland (University of Ottawa) and Dr. Laura Thomson (Queen's University) for their support, inspiration, and guidance throughout this degree. To Luke, you have been and will continue to be an exceptional mentor and I am forever grateful for all the opportunities you have provided me in the world of glaciology and academia. To Laura, thank you for your constant support and welcoming me to the Expedition Fiord family, you will always be an important mentor in my life and I would not be where I am today without you. The past two years of my young adult life have been an unforgettable journey and I am incredibly thankful for all the lessons you both have taught me.

I would like to acknowledge my thesis committee: Dr. Anders Knudby and Dr. Michael Sawada for providing helpful feedback and constant support throughout the thesis process.

I would also like to thank my fellow members of the Laboratory for Cryospheric Research (University of Ottawa) and the Ice, Climate, and Environment Laboratory (Queen's University) for their guidance and constant support throughout this project. I appreciated your company and encouragement in the field and friendship back in the lab.

Lastly, I would like to thank my friends and family for their unwavering support throughout this incredible journey. I am extremely grateful for my parents Kim and Craig Smeda for always encouraging me to work hard and never give up on my dreams. I would like to thank both of my brothers: Jakob and Tyler, who made it possible for me to be who I am. Thank you!

Table of Contents

List of Figures

List of Tables

List of Abbreviations

AHI	Axel Heiberg Island
A.S.L	Above Sea Level
CAA	Canadian Arctic Archipelago
DEM	Digital Elevation Model
DoD	DEM of Difference
dGPS	Differential Global Positioning System
ELA	Equilibrium Line Altitude
GCP	Ground Control Point
GLIMS	Global Land Ice Measurements from Space
GPR	Ground Penetrating Radar
GPS	Global Positioning System
GRACE	Gravity Recovery and Climate Experiment
GSC	Geological Survey of Canada
LST	Land Surface Temperature
MARS	McGill Arctic Research Station
NAPL	National Air Photo Library
NCAA	Northern Canadian Arctic Archipelago
PGC	Polar Geospatial Centre
QEI	Queen Elizabeth Islands
RACMO	The Regional Atmospheric Climate Model
R.C.A.F.	Royal Canadian Air Force
RGI	Randolph Glacier Inventory
SCAA	Southern Canadian Arctic Archipelago
SfM	Structure from Motion
SLC	Scan Line Corrector
SLR	Sea Level Rise
USGS	United States Geological Survey
UTM	Universal Transverse Mercator

Chapter 1

INTRODUCTION

1.1 Background and Motivation

The Canadian Arctic Archipelago (CAA) comprises the world's largest volume of glacier ice outside of the Greenland and Antarctic ice sheets (Sharp *et al*., 2011; Lenaerts *et al*., 2013; Cohen *et al*., 2014; Pfeffer *et al*., 2014; Wouters *et al*., 2019). Over the past six decades, the Arctic has warmed at twice the global average, partly due to an increase in atmospheric water vapour and Arctic amplification (Sharp *et al*., 2011; Walsh, 2014). As a result, mean surface air temperatures have increased at a rate of 0.5 °C per decade on Northern Ellesmere Island, Nunavut, since the late 1940's leading to an increase in melt season length on glaciers and ice caps within Canada's Queen Elizabeth Islands (QEI) (Mortimer *et al*., 2016; Sharp *et al*., 2011, 2015).

The QEI contained ~104,000 km^2 of ice cover in the year 2000, which accounts for 25% of all land ice in the Arctic outside of Greenland and 14% of the global glacier and ice cap area (Pfeffer *et al*., 2014). Glacier surface mass balance, defined as the annual difference between mass gained by the accumulation of snow and mass lost by the ablation of ice, is primarily controlled by summer mean air temperatures (Braithwaite, 2019). Historic in-situ mass balance measurements within the QEI, together with results derived from a regional climate model (RACMO2.3: The Regional Atmospheric Climate Model), indicate that over the period 1958-1995 land ice was in a state of slightly negative mass balance (-11.9 ± 11.5 Gt year^{-1}) (Noel et al., 2018). However, between 1996 and 2015 the QEI has experienced markedly warmer conditions, resulting in a rapid increase in the mass loss of glaciers and ice caps at an average rate of 28.2 ± 11.5 Gt year^{-1}. Furthermore, recent Gravity Recovery and Climate Experiment (GRACE) measurements of the QEI analyzed by Wouters *et al*. (2019) suggest that between 2002 and 2016 enhanced glacial runoff and ice discharge to the ocean has resulted in an average of 36 ± 4 Gt year^{-1} of ice loss. This increase in meltwater runoff affects sea level rise, with the glaciers and ice caps within the CAA containing enough water to raise sea level by ~109 mm if they all melted according to Moon *et al*., 2018, or 85.3 ± 22.1 mm according to Farinotti *et al*., 2019. Projections by Moon *et al*. (2018) suggest that between 2006 and 2100 the CAA will contribute ~33 mm to global sea level rise based on the RCP8.5 emissions scenario. In addition, Box *et al*. (2018) established that between 1971 and 2017, the circumpolar Arctic has been the single greatest contributor to eustatic sea level rise (SLR), with Arctic Canada contributing 3.21 mm, third in importance after Greenland (10.61 mm) and Alaska (5.71 mm). With a significant terrestrial ice cover, and current and potential contributions to SLR, Canada's Arctic Archipelago has become an important region for glaciological research.

1.2 Focus and Objectives

This thesis investigates how Adams Icefield, comprised of three small (<1 km^2) ice bodies (Baby, Trent, and Black Crown glaciers) on Axel Heiberg Island in the Canadian High Arctic, has changed over the past seven decades (1948-2019). While small glaciers (<1 km^2) cover a small proportion of the total ice-covered area in the CAA, they demonstrate a greater sensitivity to a warming climate as a result of a shorter response time than large ice masses (Huss and Hock, 2015; Bahr and Radic, 2012). For example, recent measurements on northern Ellesmere Island have demonstrated how glaciers <1 km^2 in area lost ice at an average rate of 30.4% decade^{-1} between ~1999 and ~2015, with the complete loss of three small ice caps over this period (White and Copland, 2018). Although negligible contributors to sea level rise, small glaciers respond quickly to external climate forcing, can have a major impact on the hydrological regime in glacierized drainage basins, and are relevant for landscape formation and bedrock erosion (Huss and Fisher, 2016).

Based on the 2011 Randolph Glacier Inventory from the Global Land Ice Measurements from Space (GLIMS) database (https://www.glims.org/RGI/), ~627 glaciers exist on Axel Heiberg Island with 164 (26%) being smaller than 1 km^2 (Figure 1.1). To date, no detailed work has been undertaken to quantify the causes and patterns of the changes of these small glaciers, which limits understanding of the impacts of climate warming in this region. Using historic datasets dating from the 1940's, this thesis therefore presents a multi-decadal assessment of the mass balance, area, and volume change of Adams Icefield using a ~36-year glaciological mass balance record, optical satellite imagery, historical aerial photographs, ground penetrating radar surveys, and contemporary photogrammetry techniques. The objectives are as follows:

i. To measure the area change of Adams Icefield, composed of Baby, Trent, and Black Crown glaciers, from 1948 to 2019 on a five- to ten-year time interval.
ii. To quantify ice thickness changes and the geodetic (i.e., volume-change derived) mass balance of Adams Icefield between 1959 and 2019.
iii. To estimate how long Adams Icefield can survive into the future based on current mass balance rates and total ice volume.

The results from this project will provide a significant improvement in the understanding of the patterns of change that are occurring for small glaciers in the Canadian High Arctic, and the life expectancy of these small ice masses. The period 1948 to 2019 was selected for the focus of this study as it coincides with the availability of historical aerial photographs (1948-1977), optical satellite imagery (1974-2019), and field-based measurements (1959-2019, with gaps).

This thesis is written in a traditional-style format. The current chapter synthesizes background information about the CAA, the objectives and motivation behind this project, and the study location. A literature review chapter presents existing research on climate and glacier cover in the Canadian High Arctic. Methodology, results, and discussion chapters follow. At the end of each chapter are the associated tables and figures, and the references are all placed together at the end of the thesis.

1.3 Study Location

1.3.1 Axel Heiberg Island

Axel Heiberg Island (AHI), Nunavut, is a highly glacierized, remote, uninhabited northern island (78 to 81°N, 90 to 93°W), situated west of Ellesmere Island and separated from it by Nansen and Eureka sounds (Figure 1.2B). Located within Canada's QEI, approximately a quarter of its land area of ~43,000 km^2 is glacier covered. Based on analysis of 1959 aerial photographs, 55% of the island's ice cover consists of outlet glaciers, 26% mountain glaciers, 16% ice caps, and 3% icefields (Ommanney, 1969). Two large ice caps comprise the majority of the ice cover on AHI: (1) Müller Ice Cap, located ~50 km northeast of Expedition Fiord, and (2) Steacie Ice Cap, situated on the southern half of the island, approximately 75 km south of Expedition Fiord (Figure 1.2B). Müller Ice Cap was named after Dr. Fritz Müller of McGill University who established the glacier monitoring program in Expedition Fiord (1959/60), and who helped to found the McGill Arctic Research Station as part of the Jacobsen-McGill Arctic Research Expedition (1959-1962).

A baseline inventory of glacier cover on AHI was constructed by Ommanney (1969) in reference to 1958-59 aerial photography, which established that the island contains approximately 1,120 ice masses. Thomson *et al*. (2011) compared Ommanney's inventory against the 2000

Global Land Ice Measurements from Space (GLIMS) inventory and established that island-wide ice coverage decreased by ~15.92 km^2 over the 41-year period (1959: 11,725.22 km^2; 2000: 11,709.30 km^2). From the Ommanney inventory, 90.5% of all ice masses were classified as retreating, 2.9% were stationary, and 5.7% were found to be advancing. Although the majority of the glaciers on AHI were retreating, it was revealed that the contribution of these glaciers to overall area loss was concealed by glaciers advancing, the greatest of which was seen at Iceberg Glacier on western AHI, which increased in area by 77.81 km^2 between 1959 and 2000. There is evidence that some of these advances were due to surging (Copland et al., 2003), although it is not possible to confidently say whether this is the exclusive process that was responsible for all advances (Medrzycka *et al.,* 2019). Island-wide, 294 glaciers that were listed in the Ommanney inventory ceased to exist in the GLIMS (2000) inventory, suggesting that 26% of all glaciers identified by Ommanney (1969) are no longer present or are undetectable by the satellite remote sensing approaches used for GLIMS. Based on recent air photo surveys and observations from optical satellite imagery in 2009, Thomson *et al*. (2011) determined that 165 glaciers had disappeared completely while 128 glaciers from Ommanney's 1959 inventory had shrunk to an area less than 0.04 km^2 (the smallest glacier area accepted in the GLIMS inventory), and were therefore not registered in the 2000 GLIMS inventory.

1.3.2 Expedition Fiord, Axel Heiberg Island

Established in 1960, McGill University owns and operates the McGill Arctic Research Station (nicknamed "MARS"), which is situated ~8 km inland of Expedition Fiord (Figure 1.2A), in central-western AHI (79°42'N, 90°75'W). Presently, MARS is one of the longest operating field research stations in the Canadian Arctic, and has been used to access nearby White Glacier to produce the one of the longest continuous mass balance records (1959-2019) for an alpine glacier within the High Arctic (Figure 1.2A), tied with Meighen Ice Cap. White Glacier (79°45’N, 90°53’W) is a 14-km long mountain glacier extending from 100 to 1,800 m a.s.l. Between 1960 and 2014 it decreased in area by ~2.53 km^2, from 41.07 km^2 to 38.54 km^2 (Thomson and Copland, 2016). White Glacier’s most recent decadal mean glaciological mass balance has been the most negative over the past ~60 years, with 8 of the 10 most negative mass balance years occurring since 2000 (Thomson *et al.*, 2017).

1.3.3 Adams Icefield, Expedition Fiord

Adams Icefield is comprised of three small ice bodies: Baby Glacier, Trent Glacier, and Black Crown Glacier (Figure 1.3). Baby Glacier (79°26’N, 90°40’W) has been the subject of glaciological research since 1959 and hosts a sporadic in-situ mass balance record lasting ~36 years (Adams *et al.*, 1998). Baby Glacier is classified as a high-elevation niche glacier, which partially fills the v-shaped valley between Wolf Peak and Black Crown Peak (Figure 1.3), located on the northern perimeter of Expedition Fiord (Figure 1.2A).

Black Crown Glacier is situated on the northern slope of Wolf and Black Crown peaks with an approximate area of 1 km^2, whereas Trent Glacier is found in a v-shaped valley on the western slope of Black Crown Peak, directly west of Baby Glacier (Figure 1.3). Located northwest of MARS basecamp in a south-southwesterly exposure, Ommanney (1969) estimated Baby Glacier’s mean thickness to be ~15 m with an approximate area of 0.61 km^2 determined from oblique aerial photographs collected in August 1959. Due to its thin ice cover, high elevation, and high northern latitude, Baby Glacier is classified as a cold polar glacier (Adams *et al.*, 1998), meaning that it`s likely frozen to its bed.

Although unofficial, Adams Icefield is commemoratively named after W.P. Adams who passed away in 2018. Adams assisted in developing and maintaining the mass balance program in Expedition Fiord, particularly on Baby Glacier.

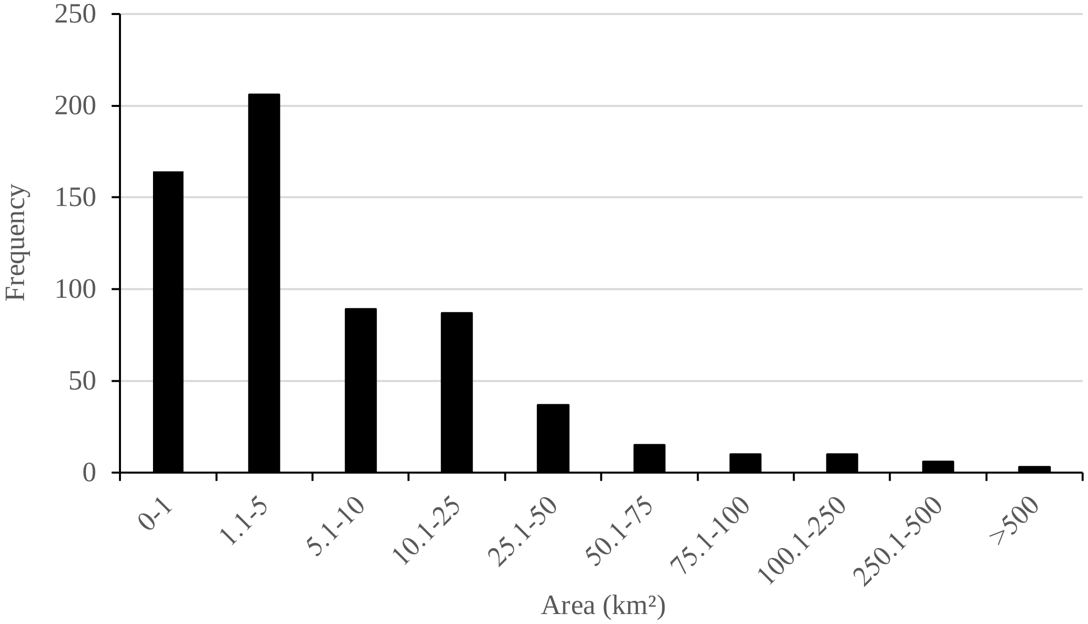

Figure 1.1. Distribution of glacier size (km^2) and frequency on Axel Heiberg Island, Nunavut, based on the 2011 Randolph Glacier Inventory.

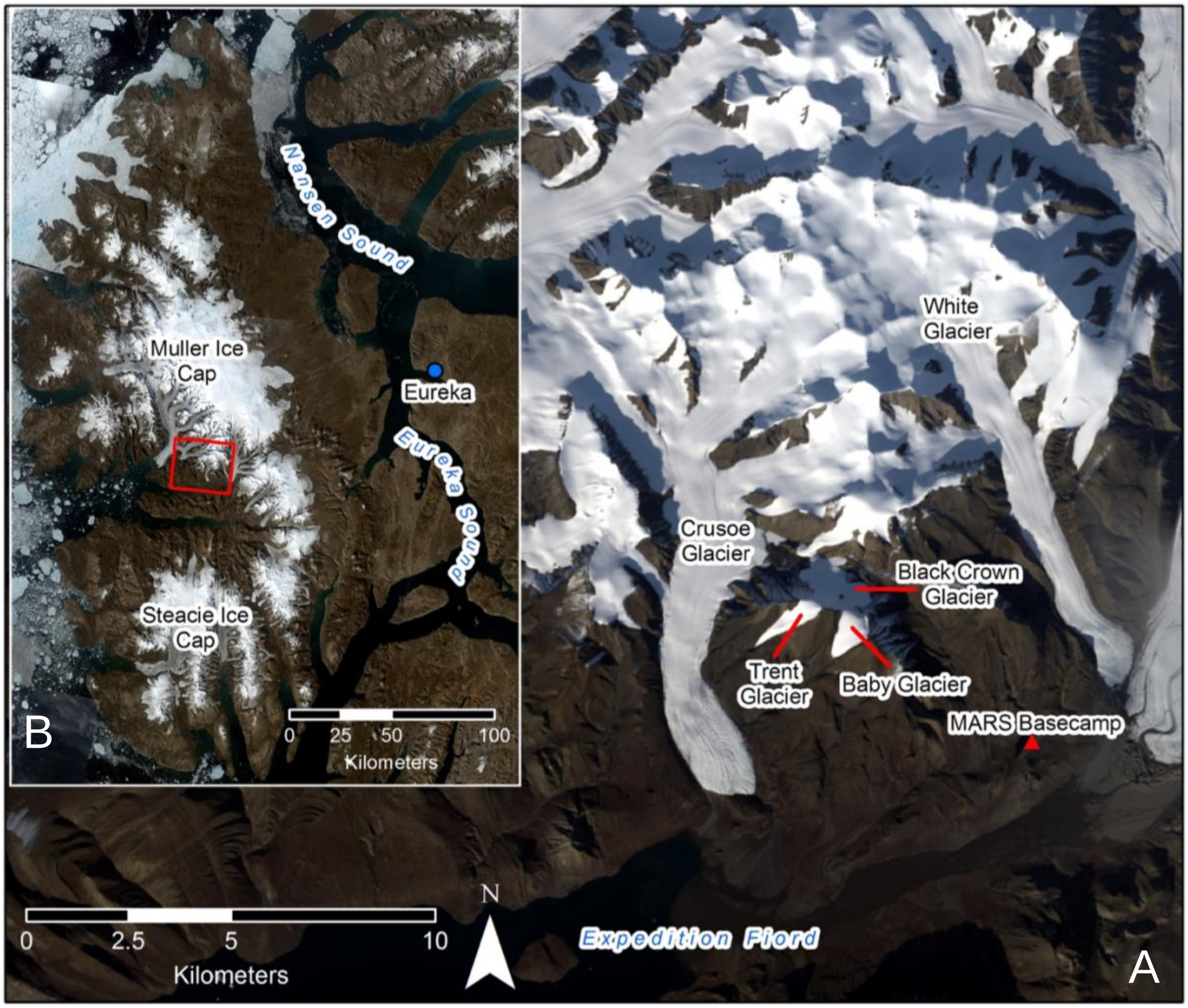

Figure 1.2. A: Map of Expedition Fiord, Axel Heiberg Island (AHI), Nunavut; B: Location of Expedition Fiord on AHI. Base Image A: Sentinel-2 optical satellite imagery (September 1, 2015); B: Mosaic of Sentinel-2 optical satellite imagery (August, 2019). MARS: McGill Arctic Research Station.

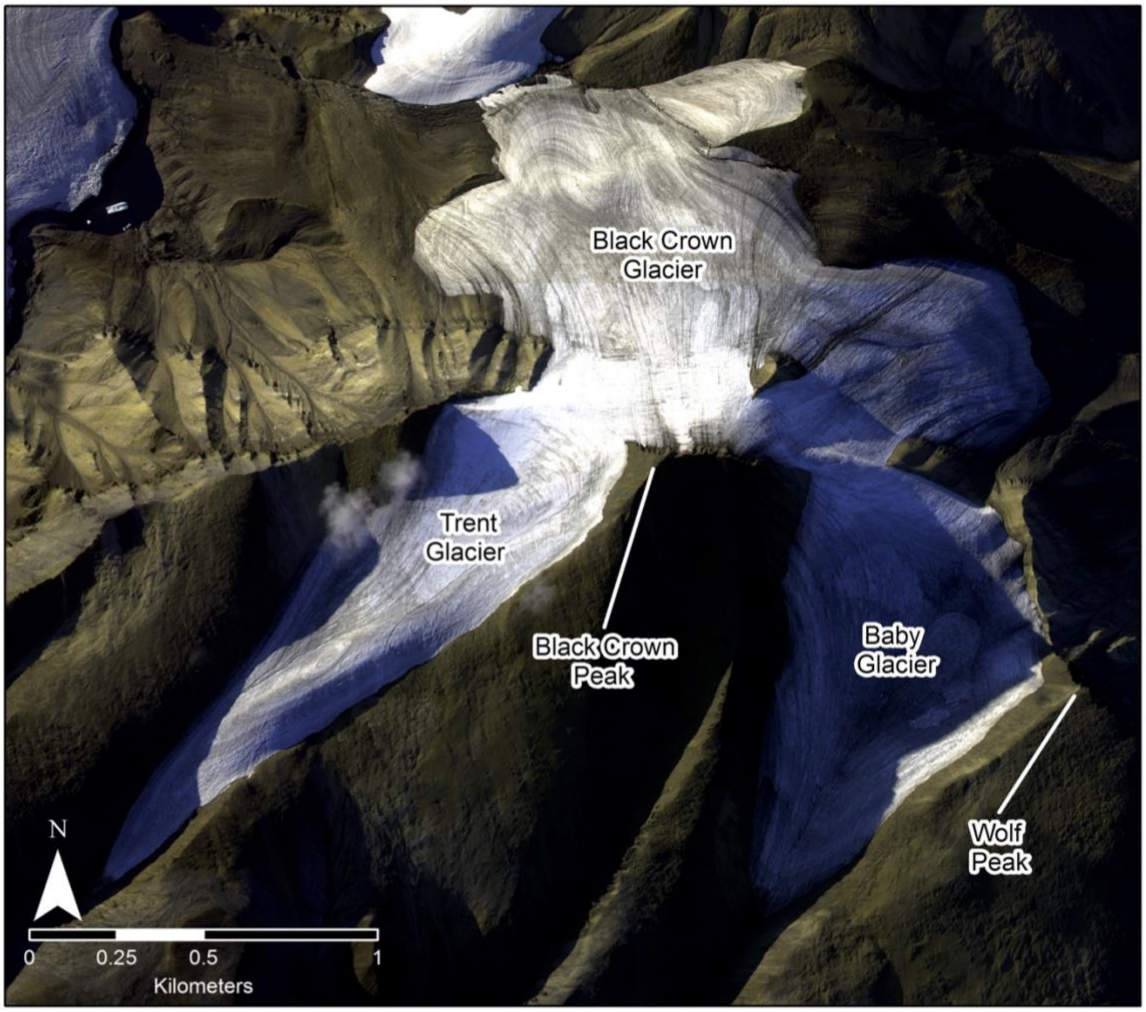

Figure 1.3 High-resolution (30 cm) WorldView-2 satellite scene of Adams Icefield, August 11, 2012.

Chapter 2

LITERATURE REVIEW

2.1 Glacier Change in the Canadian Arctic Archipelago

Most glaciers and ice caps within the QEI are found on Axel Heiberg, Devon, Ellesmere, and Meighen islands; this region is also called the Northern Canadian Arctic Archipelago (NCAA). The Southern Canadian Arctic Archipelago (SCAA) comprises several islands, with the majority of glaciers and ice caps located on Baffin and Bylot islands. The NCAA contains ~104,000 km^2 of ice cover (RGI Consortium, 2017), which is characterized by many small ice caps and glaciers (see Figure 1.1), several large ice caps and icefields (e.g., Devon, Prince of Wales, Agassiz, Manson), and numerous marine-terminating outlet glaciers which discharge ~2.2 ± 0.7 Gt year^{-1} of ice to the ocean (mean for 2000 and 2011-2015) (Van Wychen *et al*., 2016). The SCAA contains ~42,000 km^2 of ice cover (RGI Consortium, 2017), dominated by land terminating glaciers, and therefore calves significantly less ice into the ocean than the NCAA at an average rate of 0.06 Gt year^{-1} between 2007 and 2011 (Van Wychen *et al*., 2015; Noel *et al*., 2018). Recent GRACE measurements illustrated that between 2002 and 2016, the NCAA (QEI) lost ice mass at a rate of 36 ± 4 Gt year^{-1}, while the SCAA lost 32 ± 8 Gt year^{-1} (Wouters *et al*., 2019).

In-situ mass balance observations began in the Canadian Arctic in the early 1960's, and since then the most negative balance years have occurred since 2005 (Wolken *et al*., 2017). Surface mass balance measurements have been monitored on several ice masses within the CAA: Devon, Agassiz and Meighen Ice Caps, monitored by the Geological Survey of Canada (GSC), and White Glacier, currently monitored by Queen's University and the University of Ottawa. According to Koerner (2005), with the exception of Meighen Ice Cap, there was a growing trend of increasingly negative mass balances for all monitored ice masses within the Canadian Arctic between 1980 and

2000. Koerner (2005) attributed these increasingly negative mass balances to warmer summer surface air temperatures, which intensified glacial surface runoff. From 1971 until the mid-1980s, the CAA's glacier mass balance was relatively stable (Figure 2.1). However, there was an acceleration in mass losses in this region between ~1986 and 2012. In 2013, there was an anomalously slightly positive year for Arctic Canada, illustrated by the dip on the right side of Figure 2.1 (Box *et al*., 2018).

2.2 Contributions to Sea Level Rise from the Canadian Arctic Archipelago

Farinotti *et al*. (2019) used ice thickness modelling to estimate that the CAA currently contains 36.94 ± 9.58 x 10^3 km^3 of glacier ice, equivalent to 85.3 ± 22.1 mm of sea level rise if it all melted, most of which is locked up within the QEI (64.8 ± 16.8 mm). Moon *et al*. (2018) estimated that the CAA contains enough ice to raise sea level by ~109 mm. Between 2003 and 2009, Moon *et al*. (2018) reported that 60 Gt $year^{-1}$ of ice was lost from the Canadian Arctic, of which 33 Gt $year^{-1}$ occurred from the QEI. Similarly, between 2002 and 2016, Wouters *et al*. (2019) reported that a total of 68 Gt $year^{-1}$ of ice was lost from the Canadian Arctic.

Surface mass balance changes due to meltwater runoff are dominating glacier losses in the Canadian Arctic when compared against ice discharge to the ocean (Van Wychen *et al*., 2014; Millan et al., 2017). Between 1991 and 2005, the QEI lost mass at a rate of 6.3 ± 1.1 Gt $year^{-1}$, with ice discharge to the ocean (i.e., iceberg production) contributing 55% of these losses (3.4 ± 0.1 Gt $year^{-1}$), followed by meltwater runoff (3.0 ± 1.1 Gt $year^{-1}$). However, since then the mass budget has become increasingly negative due to an increase in surface meltwater runoff (-55.6 ± 16.6 Gt $year^{-1}$ in 2012), with ice losses due to ice discharge to the ocean contributing only 10% of the total (Millan *et al*. 2017). Arctic glaciers and ice caps are currently contributing 0.5 mm year^{-1} to sea level rise, with the QEI contributing 0.09 mm year^{-1} between 2003-2009 (Moon *et al*., 2018).

According to the RCP4.5 moderate warming scenario (where global mean near-surface temperatures increase by ~3.5°C by 2080), CAA glaciers could potentially lose ~18% of their volume by 2100. This would provide an increase in sea level of approximately ~0.35 ± 0.24 mm year^{-1} (Lenaerts *et al*., 2013). Similar projections by Moon *et al*. (2018) indicate that Canadian Arctic glaciers will contribute a total of ~33 mm to sea level rise by the end of the 21st century.

2.3 Influence of Elevation on Glacier Mass Balance in the High Arctic

Small ice masses at high northern latitudes are particularly sensitive to a warming climate given their large area to volume ratio, and potential to completely lose their accumulation area if the equilibrium line altitude (ELA) rises above the top of their basin. The ELA, defined as the elevation at which mass balance is equal (i.e., where the annual accumulation of snow and refrozen meltwater is balanced by the annual ablation of ice), is an important variable to consider when discussing mass balance changes of glaciers. This is particularly true for small glaciers and ice caps, as these ice masses have a greater chance of being either completely above or below the ELA compared to larger ice masses.

Braun *et al*. (2004) studied changes of four ice caps on the Hazen Plateau on northeastern Ellesmere Island from 1959 to 2002. This region comprises a rolling upland area, with an elevation range from 300 m to >1,000 m a.s.l. (Serreze *et al*., 2017). These ice masses experienced positive mass balance years and expansion in area from the mid-1960s until the mid-1970s, but from the 1980's onwards they experienced negative mass balance conditions and a reduction in area (total area losses of 30-47% for all four ice caps since 1959) as land surface temperatures increased, increasing the ELA (Braun *et al*., 2004). Serreze *et al*. (2017) further confirmed these results when studying two Little Ice Age relic ice masses within St. Patrick's Bay on the Hazen Plateau. Both ice caps decreased to 5% of their original 1959 area (7.48 km^2 and 2.93 km^2) over the 56-year period 1959 to 2015. As well, Serreze *et al*. (2017) studied the Murray and Simmons ice caps (also located within the Hazen Plateau), which decreased to 39% (Murray) and 25% (Simmons) of their original 1959 area. This is attributed to their higher elevation (~200-300 m above the St. Patrick Bay ice caps) and relatively cooler summer conditions.

White and Copland (2018) analyzed the relationship between glacier area change and terrain on northern Ellesmere Island, and discovered that glacier size and elevation had significant impacts on area change over the period 1999-2015. The highest shrinkage rates occurred on small, short, low elevation glaciers. For example, ice masses that lost area at >50% $decade^{-1}$ had initial areas <5.4 km^2 and a maximum elevation of 1676 m a.s.l. As well, the largest area changes occurred from land-terminating glaciers that were <1 km^2 in area, with a mean loss of 30.4% per decade. This trend has also been noted on Agassiz Ice Cap, Prince of Wales Icefield, and Axel Heiberg Island by Sharp *et al*. (2014).

2.4 Historical Measurements of Baby Glacier

Dr. Fritz Müller, the Swiss glaciologist who initiated the research program at Expedition Fiord, selected Baby Glacier as an index for small-sized (<1 km^2) glaciers within the Canadian High Arctic (Cogley and Adams, 2000). Detailed mass balance measurements such as distribution of winter precipitation, spatial patterns of melt, formation and melt of superimposed ice, and net annual mass balances were made on Baby Glacier in support of this work between 1959-1977 and 1989-2007 (Figure 2.2). Due to the restriction of firn to higher areas within the saddle near the top of the glacier, and supraglacial streams within the saddle, Adams *et al*. (1998) proposed that Baby Glacier sat below the regional equilibrium line in 1959. However, the following year (1960-61) winter accumulation was more substantial, resulting in superimposed ice forming within the snowpack which reduced mass loss. This indicated that 1960-61 was a year of mass gain as an accumulation area existed on the small land terminating glacier. Between 1959 and 1977, Baby Glacier experienced 12 years of mass gain and 7 years of mass loss (Figure 2.2). In contrast, between 1989 and 2007 Baby Glacier experienced 2 years (1996 and 2002) of mass gain and 14 years of mass loss.

White Glacier, located ~5.5 km northeast of Baby Glacier, was established as Müller's index for medium-sized glaciers within the CAA. Mass balance measurements between the two glaciers are comparable and are often used to estimate the mass balance conditions within the Expedition Fiord region. Mass balance measurements of Baby Glacier between 1959 and 2005 indicate a mean mass loss of 150 mm w.e. year^{-1} for the years when measurements were made, while mass balance measurements of White Glacier over the same period (when measurements were also made at Baby Glacier) indicate a mass loss of 175 mm w.e. year^{-1} (Cogley *et al*., 2011).

2.5 Climate in the Canadian High Arctic

It has been widely reported that warming in the Arctic is occurring at a rate 2-3 times faster than the increase in global mean surface air temperatures over the past five decades (AMAP, 2017). The northern part of the CAA is characterized by polar desert conditions displaying very cold, dry winters and cool summers. The nearest long-term meteorological station to MARS Basecamp is the Eureka weather station (https://weather.gc.ca/city/pages/nu-11_metric_e.html) situated in

Eureka Sound (79°59`N, 85°86`W; 83 m a.s.l.), located on western Ellesmere Island approximately 120 km northeast of Expedition Fiord.

Since 2000 the CAA has experienced some of the warmest summer air temperatures as four of the five warmest years (since 1960) have occurred since 2004 (Gardner *et al.*, 2011). Climate data analyzed by Lesins *et al.* (2010) from the Eureka weather station established that between 1972 and 2007 surface annual average air temperatures increased by 3.2°C, representing a warming trend of 0.88 ± 0.17°C decade^{-1}. These results match those from the Goddard Institute for Space Studies (GISS; https://www.giss.nasa.gov/), as 11 weather stations north of 75° latitude had a range of warming from 1.18° to 4.7 °C over the same time period. In addition, White and Copland (2018) reported a 3.6°C increase in mean annual surface air temperatures across northern Ellesmere Island (located directly northeast of AHI) between 1948 and 2016 based on NCEP/NCAR reanalysis.

The autumn season (September to December, defined by Lesins *et al.*, 2010) exhibited the largest and most consistent warming, which is consistent with a delay in sea ice freeze-up (Lesins *et al.*, 2010). Over the past four decades (1979-2017), the annual Arctic minimum sea ice extent has decreased by 2.4% decade^{-1}, while the July-September minimum sea ice extent decreased by 7.0% decade^{-1} (Maksym, 2019). This decrease in areal extent is predominantly attributed to warming of both sea surface and surface air temperatures as warmer temperatures initiated earlier melt seasons and later freeze-up dates, allowing for longer open-water periods (Stroeve *et al.*, 2014). These open-water periods allow for increased heat absorption of the Arctic Ocean due to a lowering of the surface albedo.

Mortimer *et al.* (2016) analyzed mean summer land surface temperatures (LST) over glacierized regions within the QEI from 2000 to 2015. Over the 16-year period, mean summer glacier temperatures increased by 0.96°C (0.06° ± 0.04°C year^{-1}) with more than 90% of all glacierized regions within the QEI experiencing an increase in LST. Changes in LST occurred at more than double the rate at high elevations (>1,400 m a.s.l.) when compared against low elevation (<1,000 m a.s.l.) ice masses. As well, ice masses located at more northerly latitudes within the CAA experienced greater increases in LSTs compared to southern ice masses. However, LSTs regularly reached the melting point during the summer at low elevations, which resulted in melting, runoff, and mass loss of glaciers and ice caps. As well, increases in LST promotes grain growth within the glacier surface, lowering the surface albedo, which increases surface melting and leads to rapid release of impurities within the ice or snow. These impurities concentrate on the glacier surface and further aid in lowering the albedo (Flanner *et al*., 2007). This impacts surface melt rates by increasing the absorption of shortwave radiation, which is the largest source of melt energy in the QEI in summer (Mortimer and Sharp, 2018). Between 2001-2016 the mean LST over glaciers in the QEI increased by 0.049 ± 0.038 °C year^{-1} due to the positive albedo feedback, increasing the rates of mass loss.

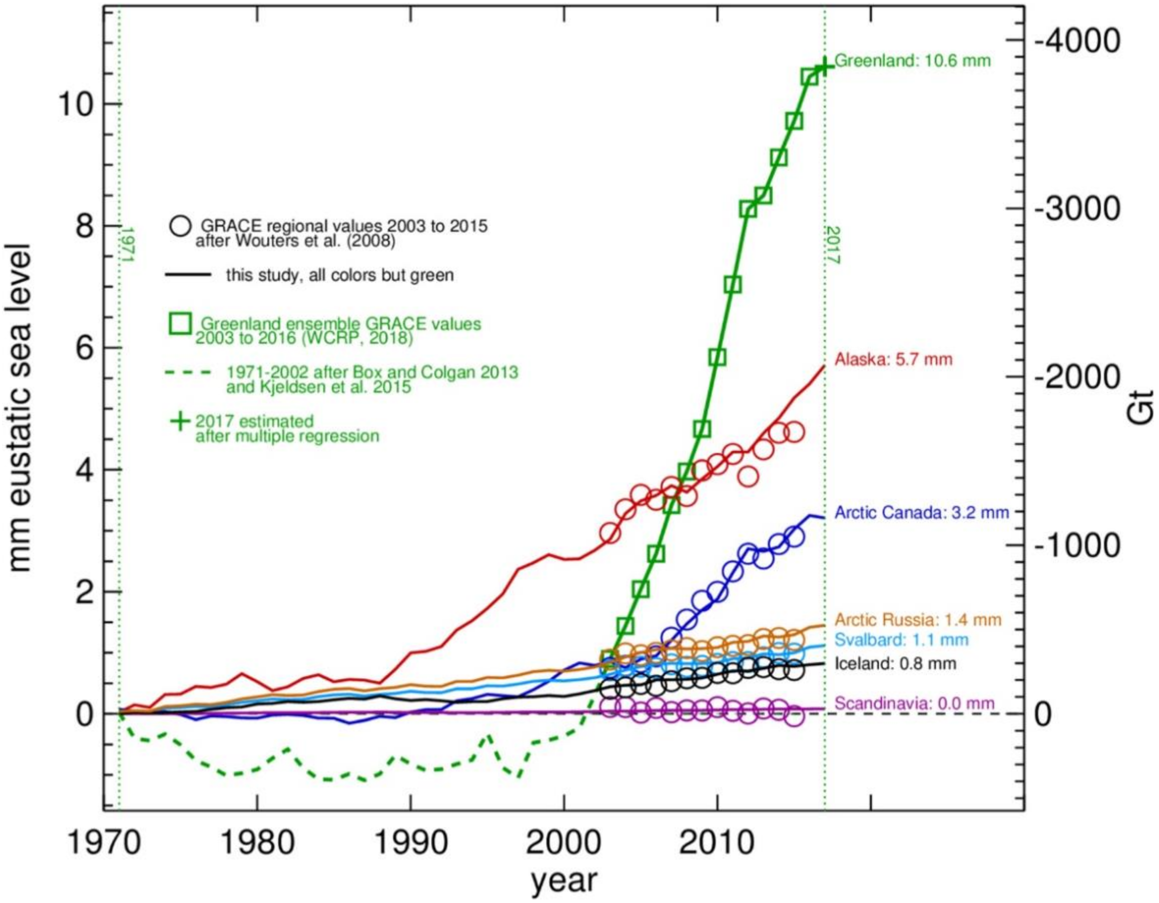

Figure 2.1. Arctic land ice cumulative sea level contribution outside of the 2003-2015 GRACE period (circles or squares) derived from scaling of regional standardized composites of in-situ mass balance measurements (Box *et al*., 2018). Note that values for Arctic Canada are indicated by the royal blue line.

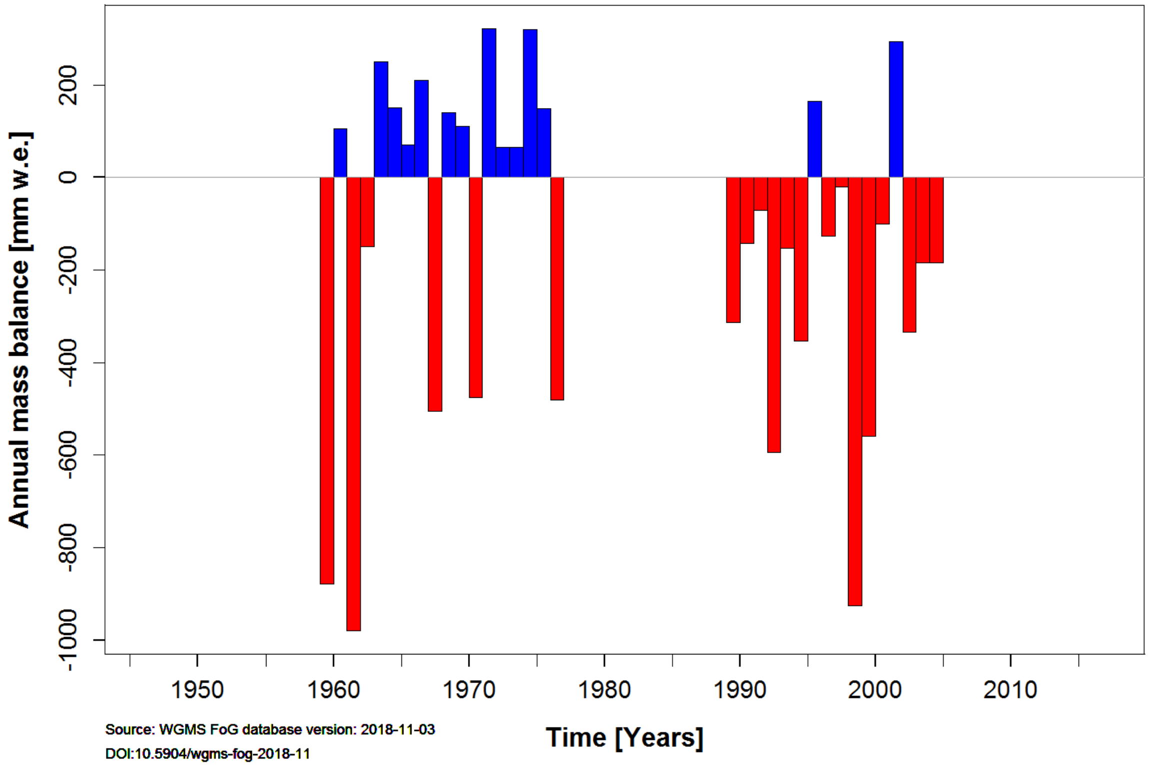

Source: WGMS FoG database version: 2018-11-03
DOI:10.5904/wgms-fog-2018-11

Figure 2.2. Annual mass balance (mm w.e.) of Baby Glacier over 36 years of measurements between 1959 and 2007. Accessed from the World Glacier Monitoring Service (DOI: 10.5904/wgms-fog-2018-11).

Chapter 3

DATASETS AND METHODOLOGY

This project used a combination of historical aerial photographs, high-resolution optical satellite imagery, geodetic mass balance measurements, and a ground penetrating radar survey to determine area and volume changes of Adams Icefield over the past 60+ years, from measurements as early as 1948. Variations in area were quantified through the analysis of historical aerial photography and optical satellite imagery. Changes in mass balance and volume were computed using Digital Elevation Models (DEMs) derived from remote sensing stereo pairs (ArcticDEM and ASTERDEM), and from air photos using the photogrammetry technique Structure from Motion (SfM). Further details of these methods are provided below.

Unless otherwise stated, all GIS analyses were undertaken using Esri's ArcGIS (Version 10.6), and DEM generations were undertaken in Agisoft Metashape Professional (Version 1.5.1).

3.1 Methods for Determining Area Change

3.1.1 Data Source: Satellite Imagery

The extent and area change of Adams Icefield was measured using optical satellite imagery from Landsat-1/5/7/8, ASTER, WorldView-2/3, and Sentinel-2 satellite sensors. Landsat and Sentinel scenes were acquired via the United States Geological Survey (USGS) through the online database EarthExplorer (https://earthexplorer.usgs.gov/) from 1974 to 2019, ASTER scenes were obtained via NASA's EarthData website (https://urs.earthdata.nasa.gov/), while WorldView scenes were provided by the DigitalGlobe Foundation. Each satellite sensor offered imagery for specific time periods with varying degrees of resolution (Table 3.1).

In May 2003 the Scan Line Corrector (SLC) failed on Landsat-7, which compensated for forward motion. As a result, each Landsat-7 scene from 2003 onwards contains missing data (black bands) resulting in incomplete imagery. To ensure the highest possible accuracy when delineating the glacier extents of Adams Icefield, multiple Landsat-7 scenes with different path and row numbers from the same summer were therefore mosaicked together for each year between 2003-2013 using the ArcGIS "Mosaic" tool from the Data Management toolbox, which enabled filling of these data gaps. Landsat-8 imagery was used between 2013-2019, supplemented by Sentinel-2 imagery after 2015.

Satellite scenes were selected on an approximately 5-year interval between 1974 and 1999, while scenes were downloaded for each individual year between 2000 and 2019 when available. Landsat, ASTER, WorldView, and Sentinel-2 sensors collect optical data which is unable to penetrate cloud cover and requires daylight to see the Earth's surface, meaning that acquisitions can be sporadic. Satellite imagery was preferentially collected from late summer (August and September), when there is minimal snow cover. Snow cover has the ability to mask a glacier's extent, making it challenging to delineate the perimeter of ice as illustrated in a 1972 Landsat-1 scene (Figure 3.1A). As a result, certain years with imagery were skipped if snow concealed the glacial extent of Adams Icefield. All optical satellite imagery was downloaded in Level-1 (orthorectified) GeoTIFF format and projected into Universal Transverse Mercator (UTM) zone 15N (NAD1983 datum, GRS80 ellipsoid) projection using the "Project" tool within the ArcGIS Data Management toolbox.

3.1.2 Data Source: Historical Aerial Photography

To delineate the extent of Adams Icefield prior to 1972 (when optical satellite imagery became available), historical aerial photography from the National Air Photo Library of Canada and the National Archives of Canada were used.

The earliest aerial photographs of Adams Icefield were taken in 1947 and 1948 during Operation Polaris by the U.S. Army Air Force trimetrogon survey (Figure 3.2A and B). This air survey involved the use of three individual cameras; one camera pointed nadir and one camera pointed to either side of the flight path positioned at an angle of ~30°. The trimetrogon flights were flown at altitudes ranging from 19,500 to 22,000 ft (5,944 to 6,706 m) above sea level, allowing each set of three images to cover an approximate area of 14 km x 14 km of the Earth's surface (Cogley and Adams, 2000). The Royal Canadian Air Force (R.C.A.F.) repeated this survey in 1950 and 1952 (Figure 3.2C and D) following similar flight paths to the 1947/48 trimetrogon surveys.

Nadir aerial images were taken across AHI in 1958 and 1959, which Ommanney (1969) used to create his detailed baseline inventory of AHI's ice masses. The Expedition Fiord region has been photographed sporadically over the six decades since then, with historical photography available from 1960, 1967, 1972-75, and 1977-78 (Cogley and Adams, 2000). More recently, air photos were taken in 2019 for this study, as discussed in Section 3.2.1.3. Historical imagery is available through the National Air Photo Library, which has been used to create numerous maps of glacier termini within Expedition Fiord such as White (1:10,000 scale), Baby (1:5,000) and Thompson (1:5,000 scale) glaciers. As a result, the historical aerial photography available for Baby, Trent, and Black Crown glaciers ranges from 1948 to 1978. Historical photographs from 2 different years (1948 and 1959) were used for this project (both examples are illustrated in Figure 3.3), in combination with photos from the 2019 survey.

3.1.3 Methods for Delineating and Calculating Ice Area

Changes in the areal extent of Adams Icefield were determined using georectified aerial photographs (1948 and 1959) and optical satellite imagery from Landsat-1/5/7/8, WorldView-2, and Sentinel-2, all scenes in nadir orientation. Both the aerial photographs and satellite imagery were georeferenced against a target image (Sentinel-2A, August 15, 2019; Figure 1.1). This Sentinel-2A scene was used as the base image for this study, as it was the most recent, high-resolution (10 m), snow free image available of Adams Icefield. The images were processed by first projecting the data (North American Datum of 1983 (NAD 83), Universal Transverse Mercator (UTM) Zone 15N) and then performing a shift to align all images to the 2019 Sentinel-2 target image. Both the 1948 and 1959 aerial photographs were georectified using a total of 5 ground control points (GCPs) (TRT, PHR, POO, WLF, and KNO; see Section 3.2.1.4 for details).

To determine the change in glacier area over time, the extent of Adams Icefield was digitized from each aerial photograph and satellite scene at a scale of 1:12,000 using the “Draw” tool within the ArcGIS editor toolbar. A minimum of 200 vertices were used when drawing each extent, generating a perimeter of each glacier, nunatak, and the icefield as a whole. All manually delineated extents were transformed into a polygon using the “Feature to Polygon” tool via the Data Management toolbox, which allowed for area (km^2) to be computed using the “Calculate Geometry” tool located within the raster’s attribute table. The digitized polygons produced from each photograph and satellite scene were then differenced to determine change in area over time. A nunatak located in the middle of Black Crown Glacier was also outlined, using the same methodology used for calculating icefield area (Figure 1.2). All nunatak areas were then subtracted from the total glacier area to ensure that the total area of ice was computed without internal bedrock.

In order to calculate the error associated with the alignment and resolution of the satellite imagery, the methods of Hall *et al*. (2003) and Williams *et al*. (1997) were used. The method of Williams *et al*. (1997) enables determination of uncertainty in the change of ice extent in the linear dimension (m) between two satellite scenes from:

$$d = \sqrt{t_1^2 + t_2^2} + RMSE \tag{1}$$

where t_1 is the resolution (m) of the first satellite scene and t_2 is the resolution (m) of the second satellite scene, and the root mean square error (RMSE) is the error associated with the georectification of the scenes. In this study the linear uncertainty was 7.15 m. Next, to convert this linear uncertainty into an area uncertainty, the method of Hall *et al*. (2003) was used

$$a = A(\frac{2d}{x}) \tag{2}$$

where $A = x^2$ and x = the linear uncertainty calculated in equation 1 (7.15 m). This calculation produced an area error of ±0.0001 km^2.

3.2 Methods for Determining Volume Change and Mass Balance

The geodetic mass balance method determines glacier-wide volume changes by the differencing of digital elevation models (DEMs) created from airborne or satellite remote sensing surveys. The measured volume changes are then converted to mass changes using an assumed density of 850 ±60 kg m^{-3}, as discussed further in section 3.2.1.9 below. The glaciological method is effective for capturing interannual variability, with sometimes large mass balance errors (± 250 mm w.e. year^{-1}), whereas the geodetic method blends several years of mass balance data with the potential for reduced errors if accurate surface DEMs are available (Thomson *et al*., 2017; Zemp *et al*., 2019).

3.2.1 Quantification of Geodetic Mass Balance

To quantify volume changes of Adams Icefield, four Digital Elevation Models (DEMs) were analyzed. Three were generated for this project from 1959 nadir air photos, 2000-2004 ASTER satellite imagery, and 2019 oblique air photos. The fourth DEM was produced by the University of Minnesota Polar Geospatial Centre (ArcticDEM). The ArcticDEM is reviewed first (*Section 3.2.1.1*) as this is the target dataset against which the others source DEMs were coregistered against, followed by the ASTERDEM (*Section 3.2.1.2*) and Structure from Motion DEMs (*Sections 3.2.1.6* and *3.2.1.7*). However, due to high vertical and horizontal accuracy errors, the final 1959 DEM was not suitable for analysis as described in Section 4.2.1 (Error Assessment of Digital Elevation Models).

3.2.1.1 Data Source: ArcticDEM Dataset (2016)

ArcticDEM is a high-resolution, pan-Arctic DEM dataset generated through the stereo-photogrammetric processing of panchromatic satellite imagery from the DigitalGlobe Constellation (WorldView-1/2/3 satellites) between 2012 and 2015 (Morin *et al.*, 2016). In 2018, the Polar Geospatial Centre (PGC) (https://www.pgc.umn.edu/data/arcticdem/) issued ArcticDEM Release 7 covering all land area north of 60°N latitude. In addition to providing 2 m strip DEM rasters, the PGC also constructed 2 m mosaic DEMs in which void areas were reduced through the mosaicking of multiple strip DEMs with varying acquisition dates (2011-2017). However, in order to remove any ambiguity concerning the acquisition date, and to reduce the level of uncertainty regarding the mean vertical accuracy (m) of the mosaicked elevation raster, this study used the 2 m strip ArcticDEM product.

Adams Icefield is located within the ArcticDEM strip "SETSM_WV02_20120702_103001005A052700_1030010059466E00_seg1_2m_v3.0," collected on July 2, 2012 by the WorldView-2 satellite and covering an area of ~1,864 km^2. Due to a lack of ground control points, the absolute vertical and horizontal accuracy for all strip ArcticDEM products is indicated as being approximately 4 m (https://www.vedur.is/media/frettir/ArcticDEM_Documentation_and_UserGuidance_Rel4.pdf). Altimetry offset (m) data collected from NASA's Ice, Clouds, and Land Elevation Satellite (IceSAT) sensor is provided within the metadata of each strip DEM, although these values are not applied to the final DEM product made publically available. The specified IceSAT altimetry offset for the 2012 strip ArcticDEM used in this study was 0.75 m. The 2012 ArcticDEM served as the target DEM against which the other DEMs used in this study were coregistered (*Section 3.2.1.8*). This dataset was selected as the target DEM due to its high-resolution and vertical accuracy.

In total, 16 strip DEMs overlap the extent of Adams Icefield with acquisition dates ranging from 2011 to 2016; the July 2, 2012 strip DEM was selected for this study as it was acquired in late summer when there was minimal snow cover on the glaciers, and it is not temporally near any other DEMs used in this study. A Sentinel-2A satellite scene from July 2, 2012, shows that minimal snow cover existed over Adams Icefield at this time.

3.2.1.2 Data Source: ASTER DEMs (2000-2004)

Five Advanced Spaceborne Thermal Emission and Reflection Radiometer (ASTER) DEMs were generated from 2000-2004 ASTER satellite imagery. The original Level 1A ASTER images were downloaded from NASA's EarthData website (https://urs.earthdata.nasa.gov/), and preferentially selected based on late summer and cloud free coverage of Adams Icefield (Section

3.1.1). The ASTER DEMs were chosen as they fill a significant temporal gap between the 1959 air photo DEM and 2012 ArcticDEM, allowing the identification of potential changes in the rate of ice surface elevation change over the period of record (1959 to 2019). It is particularly important to address this temporal gap as recent mass balance data in the Canadian High Arctic suggest that mass losses have increased dramatically since about the year 2000 due to warmer conditions (Wouters *et al*., 2019).

Downloaded ASTER satellite images were processed into DEMs on the Cedar high performance supercomputing cluster using MMASTER (Girod *et al.,* 2017). Once processing was complete, each of the five DEMs (2000-2004) were imported into GIS software and inspected for inaccuracies associated with cloud cover, void data, and elevation. Once inspected, an August 19, 2001 (AST_L1A00308192001200021_Z) and July 8, 2003 (AST_L1A_00307082003195228_Z) ASTER DEM were both co-registered to the 2 m 2016 strip ArcticDEM dataset. The three remaining DEMs were rejected due to large areas of void data over stable terrain and glacier ice, and early acquisition dates (i.e., April) when there was significant snow cover. As a result, they were not used further in this study.

3.2.1.3 Data Source: Air Photo Surveys (1959 and 2019)

Nadir and oblique air photographs collected over Adams Icefield in 1959 and 2019, respectively, were used to generate two DEMs using the photogrammetric technique Structure from Motion. 1959 aerial photography was collected from the National Air Photo Library as described above in Section 3.1.2. In total, 44 photographs (A16753-110 to A16864-038; Table 3.3), taken between July 13, and August 13, 1959 at an altitude of ~30,000 ft above sea level, with a spatial resolution of ~5 m and 60% overlap, were used to generate the 1959 DEM and an orthomosaic product.

On July 10, 2019, a Nikon D850 digital SLR camera (45.7 megapixels) was used to take 577 oblique images with >80% overlap from a Bell LongRanger helicopter flying at an altitude of ~1,000 ft. (300 m) above ground level (Figure 3.4). While in-flight, the hotshoe on the Nikon D850 camera was used to send a time marker to a Trimble R7 dual-frequency global positioning system (dGPS) each time the camera shutter was triggered by an intervalometer. These event markers within the dGPS data allowed for the interpolation of an x, y, and z coordinate for each photograph to an accuracy of a few tens of centimeters. The survey's dGPS data was processed using Natural Resources Canada's Precise Point Positioning service (https://webapp.geod.nrcan.gc.ca/geod/tools-outils/ppp.php).

3.2.1.4 Data Source: Ground Control Points (GCPs)

Aerial photography (both nadir and oblique), which has been in use throughout much of the 20th century in the Canadian High Arctic, can provide a wealth of historical topographic data provided a sufficient number of GCPs are available (Cogley and Adams, 2000). GCPs provide the means for orienting and relating aerial imagery to a ground coordinate system and have a significant impact on the spatial accuracy of DEMs. However, in order to extract high-quality elevation data from either historical or contemporary aerial photographs, GCPs must also be of high-quality and well-distributed within the aerial photographs (Wolf and Dewitt, 2000). Founded on recommendations from the Agisoft Metashape User Manual, approximately 10-15 GCPs are required when creating a high-quality topographical product. However, GCPs must be properly separated from one another to ensure that the spread of real-world coordinates is sufficient to tie down the dense point cloud, reducing errors. It is important that any GCP placed in the field is clearly visible within multiple aerial photographs from the air photo survey. If not, the GCPs cannot be used during the model building process, reducing the absolute accuracy of the generated DEM and orthoimage. As a result, the location and orientation of each GCP is an important consideration when determining the photo survey route, which was applied to the 2019 aerial photo survey. Once the survey was completed, additional natural GCPs were selected and collected from bedrock features that were clearly visible within the 2019 air photos.

To establish real-world coordinates for both DEMs generated from air photos (1959 and 2019), a total of ten GCPs were used, which were created from either artificial or natural materials such as prominent bedrock features. Considerably fewer GCPs were able to be used when generating the 1959 DEM compared to the 2019 DEM, due to the lack of artificial GCPs in 1959 and the lower resolution of the 1959 photos which made it difficult to identify distinctive natural features. Three of the ten GCPs were created from coloured naval flags (100 cm x 100 cm) placed on bedrock hills surrounding Adams Icefield (one placed on July 18, 2018; two placed on July 10, 2019), while an additional three were surveyed during the July 2019 field season using large irregularly shaped bedrock boulders. The location of four of the mass balance stakes drilled into Baby Glacier and visible in the 2019 air photo survey were also used as GCPs, with their location surveyed on July 30, 2018 (Figures 3.5 and 3.6). Baby Glacier is classified as a cold polar niche glacier suggesting that the glacier does not flow. Therefore, we assume that the ablation stakes did not move between July 30, 2018 and July 10, 2019. Once each GCP was placed, a Trimble R7 dGPS unit recorded its location for ~20 minutes.

3.2.1.5 Agisoft Metashape Professional

Agisoft Metashape Professional (Version 1.5.1) is a Structure from Motion (SfM) software, which can generate georeferenced dense point clouds, textured polygonal models, high-resolution DEMs, and detailed orthomosaics by applying photogrammetry principles to a set of overlapping, georeferenced, stereo-images. Unlike traditional photogrammetry, SfM photogrammetry has a quicker processing time and can utilize hundreds of photographs with accompanying GPS data, enabling the rapid generation of high-resolution DEMs and orthomosaics over large regions (Thomson and Copland, 2016). When using SfM photogrammetry, numerous iterations are needed within Metashape when developing a DEM to allow for erroneous data points to be excluded from the topographical model, and thus to increase absolute accuracy. The following text provides a description of the methodology used to generate the DEMs and orthomosaics (Figure 3.7) in this study from the two collections of aerial photography (1959 and 2019) using the SfM software, Agisoft Metashape Professional (Version: 1.5.1.).

3.2.1.6 2019 Model Building

All aerial photographs and camera positions (derived from dGPS data) were imported into Metashape and inspected for image quality. Referred to as “cameras” in Metashape, 577 aerial photographs (collected on July 10, 2019) were used to build the 2019 DEM and orthomosaic product. Masks, which are used to cover non-usable information within each camera such as excess sky, bedrock features such as mountains, glacier ice outside of the Adams Icefield region, and helicopter fuselage, were imported into Metashape and applied to each camera to assist the camera alignment process and reduce the reprojection error. Camera alignment refers to the process of identifying a specified number of tie-points (tie-point: a feature that can be identified in two or more cameras) between each camera and matching them, as well as determining the position/orientation of the camera for each image. Once the camera alignment process was completed a sparse point cloud was generated, created via the consolidation of multiple depth maps (depth map: a 3D point cloud calculated by the difference between two stereo-images, often depicted in grey scale), as well as a set of camera positions (Agisoft Metashape User Manual). Settings that were assigned during the camera alignment process were as follows: Accuracy: High; Reference Selection: NAD1983; UTM Zone: 15N; EPSG: 3159; Key Point Limit: 160,000; Tie Point Limit: 120,000.

Once the camera alignment process was completed, GCP positions, referred to as "Markers" in Metashape, were uploaded and manually positioned in each camera where a marker was visible. In order to reduce error associated with the sparse point cloud, markers were placed in multiple cameras, with a total of 10 markers identified in over 45 photographs from the 2019 survey. To further reduce error within the model building process, the sparse point cloud was then filtered, which is referred to as "optimization" in Metashape. Optimization is the process of removing non-linear deformations from the sparse point cloud, which may have occurred during the camera alignment process. Metashape accomplishes this by adjusting camera parameters, such as the tie point covariance, ultimately minimizing the total reprojection error. In this study, the sparse point cloud was manually edited to delete erroneous data points, which produced more favourable optimization results. Optimization should not undergo more than 3 iterations as the reprojection error (averaged error over all tie-points) tends to increase if the sparse point cloud is too heavily edited. A reprojection error below 0.5 pixels or less is considered perfect in Metashape and therefore was the goal for the 2019 product. After manually editing the sparse point cloud and three iterations of optimization, the final reprojection error for the 2019 DEM product was 0.32 pixels.

Once the sparse point cloud was manually edited and optimization completed, a dense point cloud was generated in Metashape. Similar to the sparse point cloud, the dense point cloud was manually edited to remove erroneous points, particularly around the edge of the cloud. Unlike the sparse point cloud, the extent (box) of the dense point cloud was selected. This procedure minimizes processing time of the DEM and orthomosaic and creates smaller file sizes. Once completed, a 3D elevation model and orthomosaic were generated from the filtered dense point cloud.

3.2.1.7 1959 Model Building

Similar to the methodology described in the previous section, 1959 nadir aerial photographs of Expedition Fiord were imported into Metashape, resulting in a total of 44 cameras. No masks were imported into Metashape as all photos were nadir and contained no airplane fuselage that needed to be removed. Settings that were assigned during the camera alignment process were as follows: Accuracy: high; Reference Selection: NAD1983; UTM Zone: 15N; EPSG: 3159; Key Point Limit: 100,000; Tie Point Limit: 80,000. Key-point and tie-point limit values were altered from the 2019 model building settings as the 1959 model contained significantly fewer cameras and therefore required fewer tie-points. Similar to the 2019 model, the 1959 sparse cloud underwent manual editing and removal of erroneous points located around the extent of the cloud to assist with the optimization process and reduce the reprojection error. Three iterations of optimization of the sparse point cloud resulted in a reprojection error of 0.8 pixels, an acceptable error as stated in the Agisoft Metashape User Manual. A 3D dense point cloud was generated from the sparse point cloud depth maps and optimized twice using the optimization tool. Once again, no more than 20% of points were removed as specified by the user manual. A 3D elevation model and orthomosaic were generated from the filtered dense point cloud.

Marker positions were inserted into Metashape for 3 GCPs (MTR, WLF, and PHR; Figure 3.5 and 3.6) during the marker projection process. Markers that represented natural features such as bedrock boulders were only able to be used as the man-made markers such as the coloured naval flags (KNO, TRT, and POO) were not in place in 1959. The combined marker accuracy error was 22 m for the 3 markers used.

3.2.1.8 Co-registering DEMs

When computing elevation differences between multiple DEMs co-registration must first occur, which refers to the vertical and horizontal alignment of two DEMs. Using topographical datasets without correcting for vertical and horizontal biases can result in erroneous volume change estimates for glaciers (Berthier *et al*., 2010). A comprehensive co-registration methodology was developed by Nuth and Kaab (2011) for studying glacier volume changes and has since become a standard procedure when performing geodetic mass balance calculations (e.g., Thomson and Copland, 2016). Shean *et al*. (2016) applied Nuth and Kaab's (2011) co-registration methodology to create an automated iterative closest-point co-registration tool in the coding software Python to co-register multiple DEMs. The technique laid out by Shean *et al*. (2016) was used to co-register the 1959/2019 photo-derived DEMs, and the ASTER DEM, against the 2-m strip ArcticDEM from August 7, 2016. Once co-registration was completed, a DEM of Difference between pairs of DEMs was calculated (*Section 3.2.1.9: DEM Differencing*).

Co-registration was based strictly on elevation differences over stable terrain (off-glacier) and addresses three potential biases: 1: shifts between DEMs in the x and y directions; 2: elevation dependent bias (z direction); and 3: biases related to acquisition geometry of datasets (Nuth and Kaab, 2011). Shifts in the x and y directions between two DEMs were solved by analyzing elevation differences and their variability with slope and aspect. Before co-registering, both DEMs were projected into the same coordinate system (NAD1983 Zone 15N), and a mask was applied to cover all glacier ice and water (such as within the fiord), leaving only stable terrain. Stable terrain with a slope of ≤ 30° was used for the co-registration process to reduce error, as suggested by Nuth and Kaab (2011). The xy shift over stable terrain was solved iteratively until the elevation difference between the un-registered DEM (source DEM) and registered DEM (target DEM = ArcticDEM) was ≤0.5 m. Unlike the xy shift, shifts in the z direction will be treated as the systematic bias, as outlined further in Section 4.2.1 (Error Assessment of DEMs).

Two important products from the co-registration process are the systematic bias (the mean offset between two DEMs after the last iteration of the co-registration process), and the random error (the standard deviation of differences on stable terrain). The systematic bias between the 2001 and 2012 DEMs was -1.277 m with a random error of 7.421 m., while between the 2012 and 2019 DEMs it was 1.106 m with a random error of 1.394 m.

3.2.1.9 DEM of Difference

The subtracting of sequential DEMs to create a DEM of Difference (DoD) is one of the most common methodologies used to quantify high-resolution volumetric change of a glacier through time. Once two DEMs have been co-registered, as described in *Section 3.2.1.8,* a DoD can be created by subtracting the temporally earlier DEM from the later DEM using equation 3:

$$\Delta E = Z_2 - Z_1 \tag{3}$$

where ΔE is the value of change in elevation (m), Z_1 is the topographical value of the early DEM and Z_2 is the topographical value of the later DEM. The resulting DoD provides reductions in ice elevation (m) as negative values, and increases in ice elevation (m) as positive values.

The differencing of multiple DEMs provides a change in volume rather than mass, but measurements of mass change are desirable for geodetic mass balance calculations and for climate impact assessments, such as calculating sea level rise contributions. In order to address this, a volume to mass conversion must be made using an assumed conversion factor. Huss (2013) proposed equation 4:

$$\Delta M = f\Delta v \cdot \Delta V \tag{4}$$

where $f\Delta v$ is the assumed density conversion. The factor $f\Delta v$ varies from study to study, but Huss (2013) suggested that a density value of 850 ± 60kg m^{-3} is best used when converting volume change to mass change. This value is based on an empirical firn compaction model adjusted for mountain glaciers, which used data from two long-term monitored glaciers in Switzerland and found that the conversion factor (fΔv) used by previous studies to be too high (by 2-15%). Earlier glaciological studies suggested an assumed density value of 900 kg m^{-3} based on Sorge's law, which advocates for zero changes in the vertical firn density profile over time (Bader, 1954). Another suggestion has been to use zonally variable density values based on the elevation band where calculations are being quantified for (e.g., 900 kg m^{-3} for the ablation zone, 500 to 600 kg m^{-3} for the ablation zone). For an observation period longer than 5-years, significant volume changes, and stable mass balance gradients, a volume to mass conversion of 850 ± 60 kg m^{-3} is suggested, which was used in this study.

3.2.2 In–Situ Mass Balance Measurements of Baby Glacier

Historical glaciological (in-situ) mass balance measurements of Baby Glacier were made sporadically between 1959 to 1977, and 1989 to 2007, as illustrated in Figure 2.2. As a result, there are approximately 36 years of data available. Specific elevations ranges were designated on Baby Glacier for the placement of these mass balance stakes.

For this study four ablation stakes were installed and their location recorded on July 28, 2018 (Figure 3.6). To stay consistent with past work conducted on Baby Glacier (Adams *et al*., 1998), historical stake names were used, ranging from E1 (accumulation band; saddle of the glacier) through to B1 (near-terminus of Baby Glacier) (Figure 3.8). Ablation stake A1 was not installed at this time as the terminus of the glacier was too steep to be safely accessed. On July 10, 2019, stake height measurements were collected at stakes E1 through B1 to determine the mass balance of the icefield for the period 2018-2019. None of the stakes were re-drilled in 2019 as sufficient lengths remained for each stake. Due to the COVID-19 pandemic the 2020 summer field season in Expedition Fiord was cancelled, so no mass balance data is available for the period 2019-2020. As well, due to time constraints the Baby Glacier mass balance measurements were not able to be calculated but exist and can be made in the future.

3.3 Ground Penetrating Radar Survey of Baby Glacier

Geophysical methods can be used to determine glacier thickness, the most common being Ground Penetrating Radar (GPR). GPR surveys provide imagery of the internal structure of a glacier, as well as an accurate shape of the glacier bed and therefore ice thickness, making GPR an important tool for understanding the state and evolution of a glacier mass balance.

During April and May 2014, Dr. Laura Thomson and M.Sc. student Michael Hackett conducted a GPR survey of Baby Glacier over three cross-transects (Figure 3.8). The collection of digital GPR profiles involves measuring the time elapsed between the transmission of high-frequency electromagnetic radar pulses into the glacier and the reflection off a subsurface feature, such as the glacier bed or an internal structure such as meltwater channel. GPR antennas with a frequency range of 1-1000 MHz are most commonly used in glaciology, with the lower the frequency, the larger the wavelength, which allows for a deeper penetration into the glacier. However, there is an inverse relationship between wavelength and spatial resolution, so low frequency antennas provide less detailed information about bed conditions and ice thickness than high frequency antennas. A PulseEKKO Pro 250 MHz antenna was used for the 2014 GPR survey, which provides a good balance between penetration and resolution in the relatively cold ice found at Baby Glacier. A single frequency GPS receiver was integrated into this system to provide location information for each trace.

Once collected, the GPR data was loaded into the software EKKO Project (Version 5.0). All three transects (Line 00, 01, and 02) were edited using a similar methodology with the following tools:

1. The GPR transect was cropped vertically from 0-1250 nanoseconds, which allowed for a maximum penetration depth of ~100 m.
2. Traces were deleted for periods when the GPR system was stationary (resulting in a flat, horizontal reflection), using the “Delete Traces” tool. A total of 19 traces were deleted from Transect 02 and 4 from transect 00. No traces were deleted from transect 01.

3. Each GPR profile was cropped horizontally using the “Crop-Horizontal” tool under Processing. This allowed for the removal of deep traces that were not relevant to identifying the glacier bed.
4. All three transects were then loaded into the LineView setting in EKKO Project, where the axis titles were added, the legend was removed, and the radio-wave velocity was set to 0.170 m ns^{-1}, an appropriate value for glacier ice in the Canadian Arctic (Copland and Sharp, 2001).

3.3.1 Cross-sectional Volume Changes of Baby Glacier

The 2014 GPR transects (Figure 3.8) were used as the basis to determine changes in the cross-sectional thickness of Baby Glacier from 1959 to 2019 for different regions of the glacier (i.e., ablation zone, mid-glacier, and accumulation zone). This was completed by collecting measurements of the elevation of the glacier bed and the adjacent valley walls for each GPR transect. The GPR data was used to determine bed elevation beneath the glacier by subtracting the ice thickness at each point from the surface elevation (in m a.s.l.) derived from the 2012 ArcticDEM. Since the GPR survey was conducted during spring 2014, which represents 2013 summer values, the 2012 ArcticDEM is temporally closest to the survey date.

Once the bedrock elevation across each transect was collected, cross-profiles of the ice thickness at each GPR transect were constructed for the surface elevations in the 2001, 2012, and 2019 DEMs. This was completed at 50 m intervals to account for noise introduced by the coarse 30 m resolution of the 2001 ASTER DEM. Due to the low quality of the 1959 DEM, accurate elevation data across each transect could not be collected, so instead a bedrock elevation point was collected at the end of each transect where the 1959 ice extent intersected the 2019 DEM.

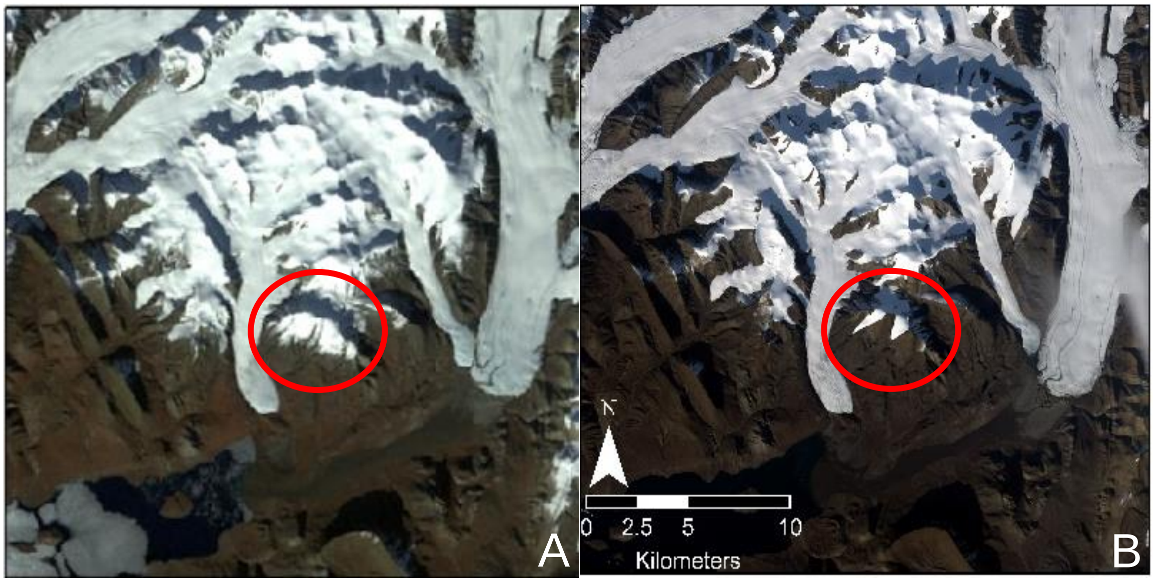

Figure 3.1. A: August 8, 1972 Landsat-1 scene of Baby, Trent, and Crown glaciers with significant snow cover; B: July 15, 2016 Sentinel-2 scene of Baby, Trent, and Crown glaciers with very little snow cover. Images obtained from USGS EarthExplorer. Red circle indicates the location of Adams Icefield.

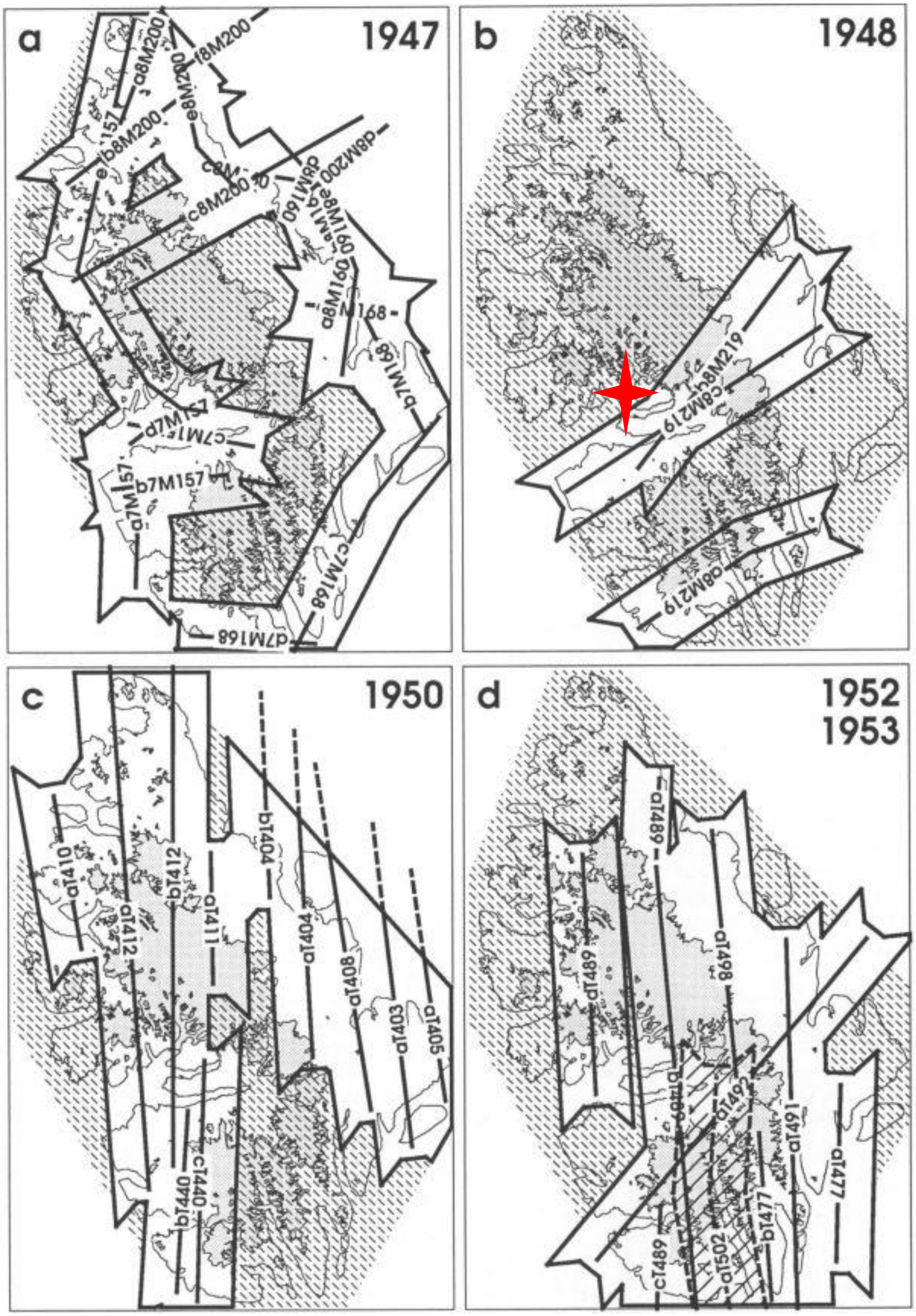

Figure 3.2. Official flight lines in which air photos of AHI were taken; A: 1947 Operation Polaris; B: 1948 Operation Polaris; C: 1950 R.C.A.F.; and D: 1952 R.C.A.F. (Cogley and Adams, 2000). Red Diamond: Location of Baby, Trent, and Crown glaciers.

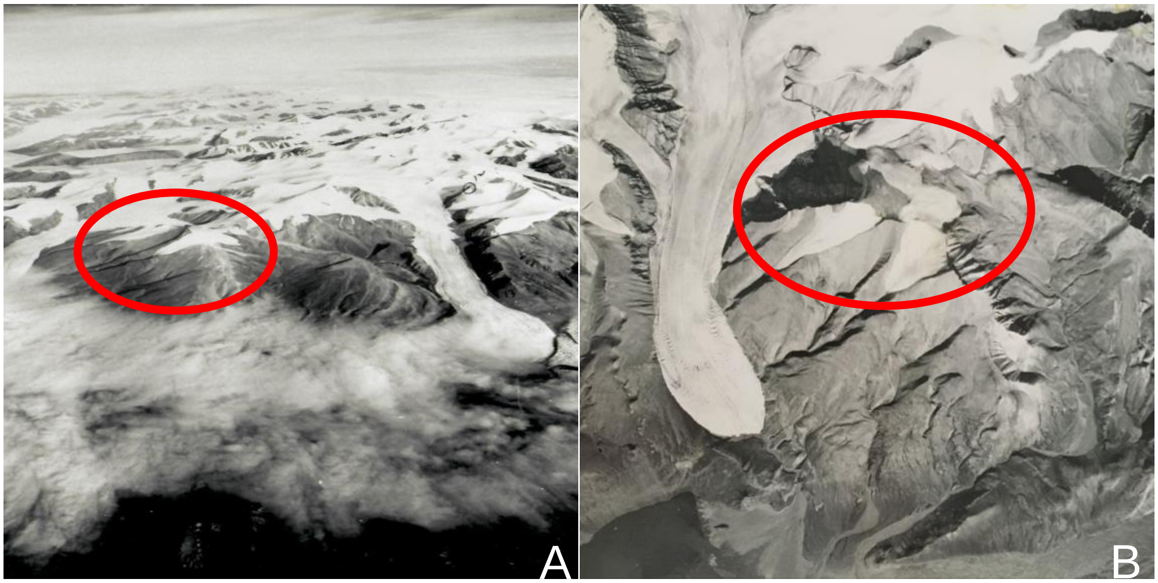

Figure 3.3. Oblique and nadir historical aerial photographs of Adams Icefield used to calculate area change. A: August 11, 1948, collected for Operation Polaris by the U.S. Army Air Force Trimetrogon Survey; B: July 28, 1959, obtained from the National Air Photo Library of Canada.

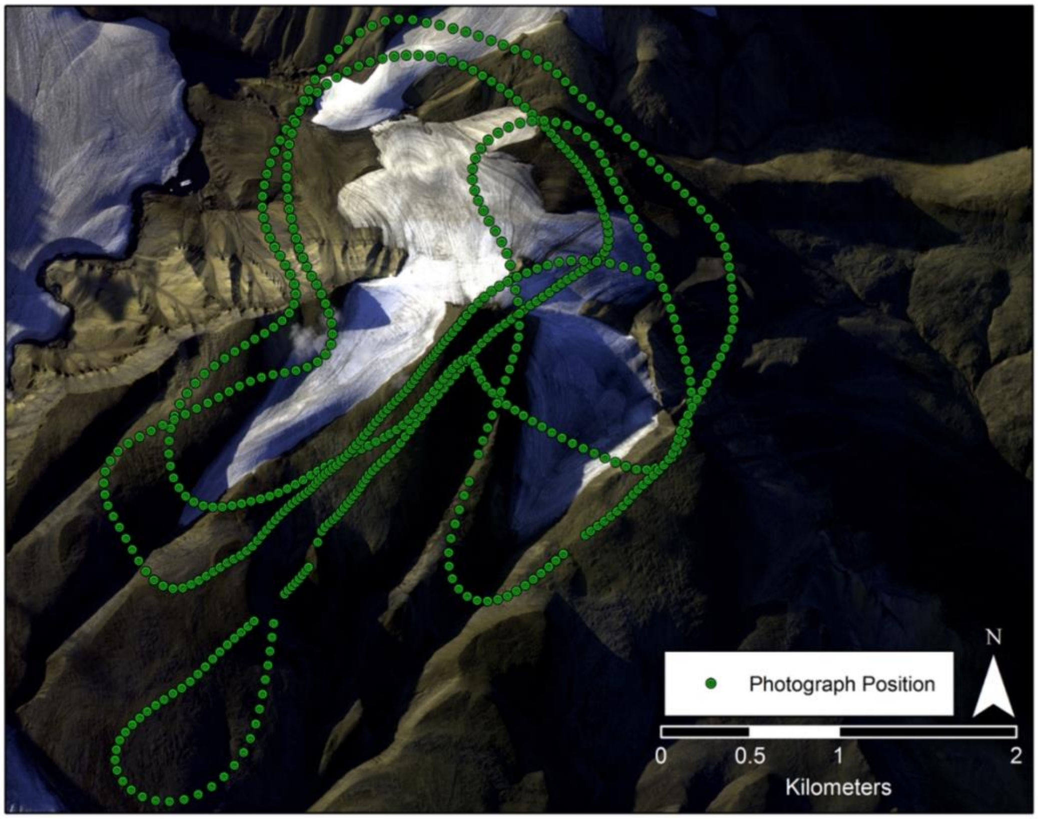

Figure 3.4. Flight path and photograph locations for the air photo survey completed on July 10, 2019. Base image: WorldView-2, August 11, 2012.

Figure 3.5. Photos of ground control points used on and around Adams Icefield in this study: A: KNO; B: TRT; C: POO; D: WLF; E: PHR; F: MTR.

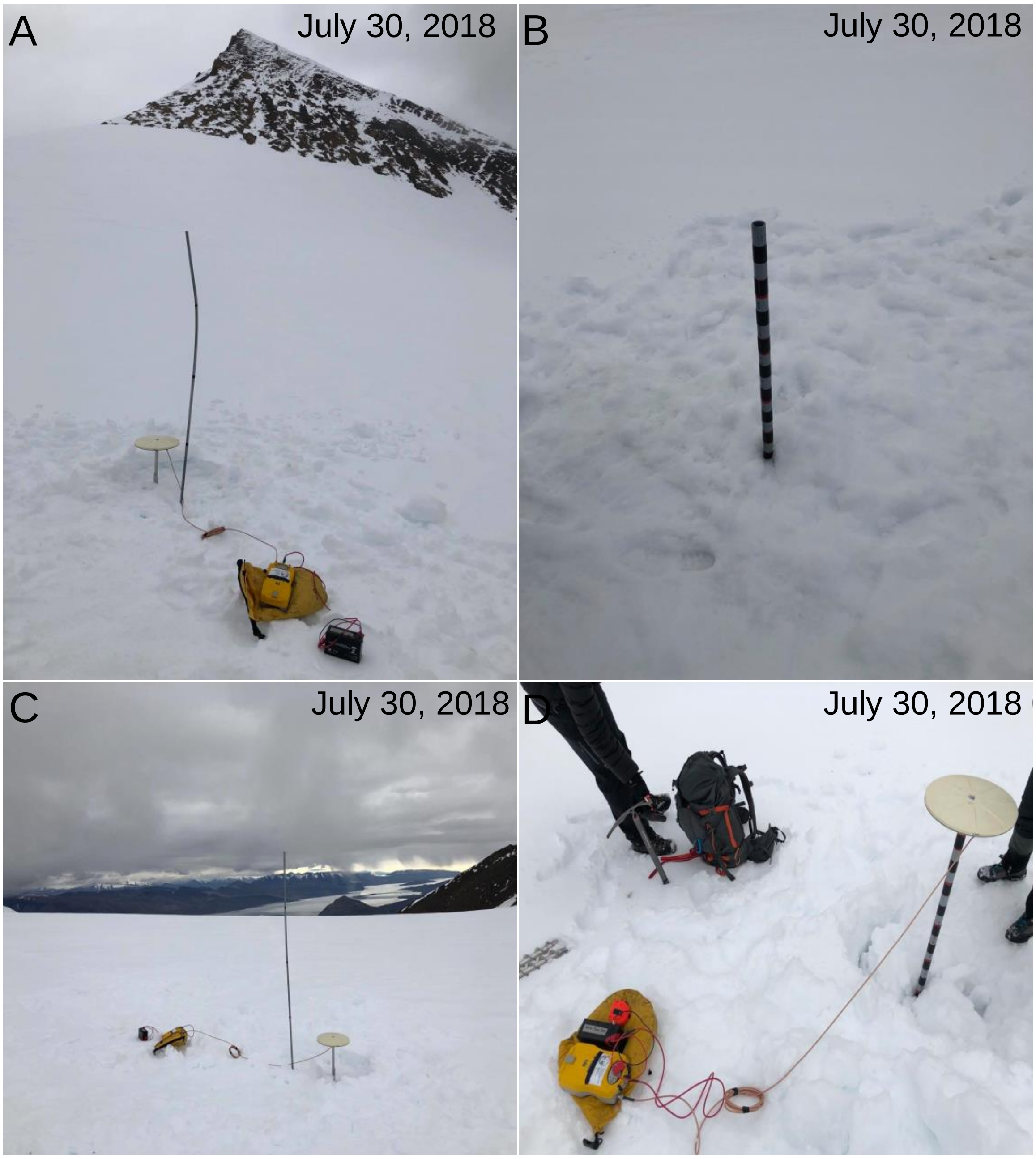

Figure 3.6. Photos of accumulation and ablation stakes installed on Baby Glacier used to assist with mass balance measurements of Adams Icefield (July 30, 2018): A: Stake E1; B: Stake D1; C: Stake C1; D: Stake B1. See Figure 3.8 and Table 3.2 for locations.

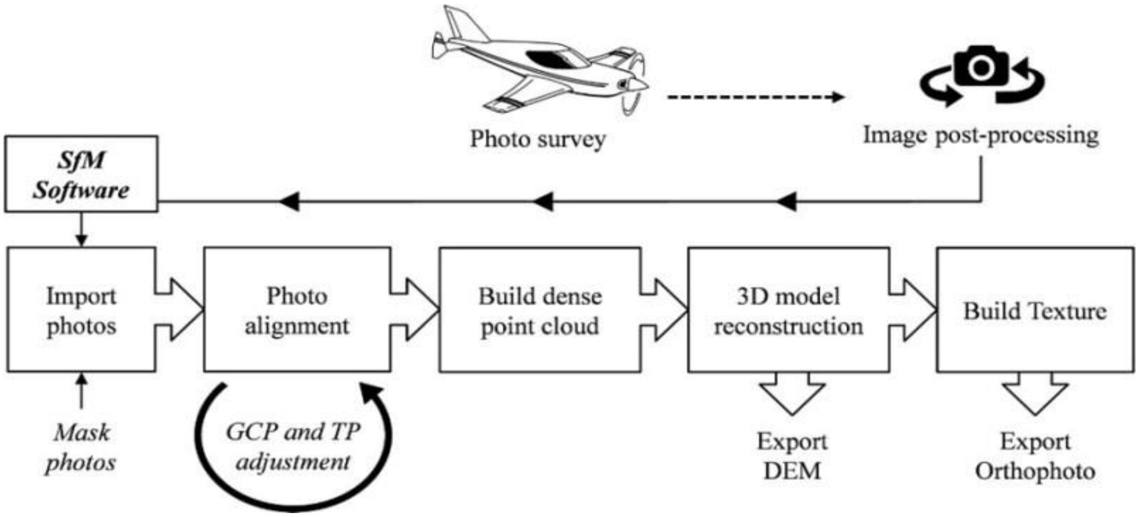

Figure 3.7. Workflow for generating a DEM using the SfM photogrammetry software, Agisoft Metashape Professional (Version 1.5.1) (reproduced from Thomson and Copland, 2016).

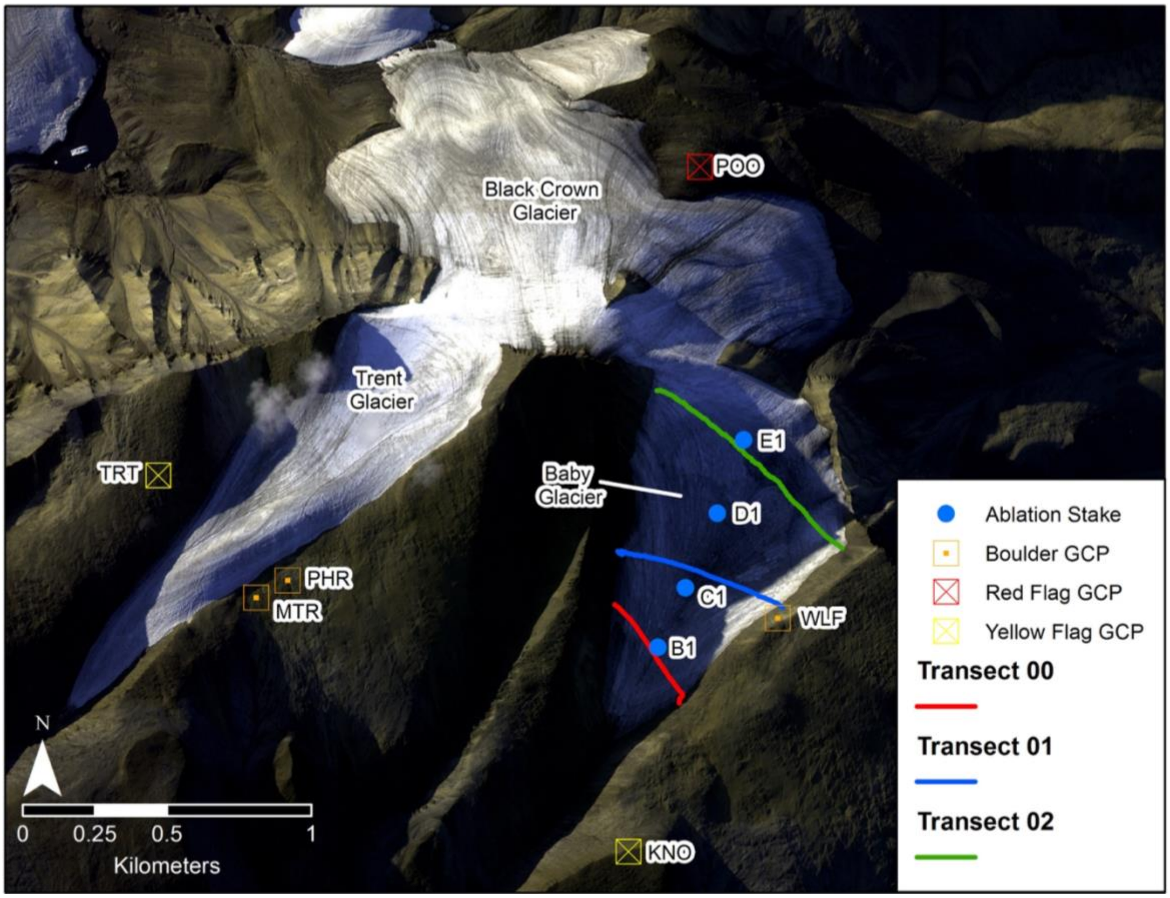

Figure 3.8. Location of all GCPs, ablation stakes, and GPR transects used for DEM production and volume change calculations. Base image: WorldView-2, August 11, 2012.

Table 3.1. Imagery used to delineate glacier extents in this project.

Sensor	**Operational Period**	**Maximum Resolution**
Landsat-1	1972-1978	80 m
Landsat-5	1984-2013	30 m
Landsat-7	1999-Present	15 m
ASTER	1999-Present	15 m
Landsat-8	2013-Present	15 m
WorldView-2	2012-Present	0.46 m
WorldView-3	2014-Present	0.31 m
Sentinel-2A/B	2015-Present	10 m

Table 3.2. Location and elevation (m) of ablation stakes placed on July 30, 2018 on Baby Glacier.

Ablation Stake	**Coordinates**	**Elevation (m)**	**2018-2019 Stake Exposure – Ice Equivalent (cm)**
E1	79.44155°N 90.95088°W	1,039	11
D1	79.43982°N 90.95838°W	1,001	20.5
C1	79.43819°N 90.96530°W	949	26
B1	79.43678°N 90.97157°W	940	39

Table 3.3. List of historical 1959 nadir aerial photographs used to generate the 1959 DEM and orthomosaic. Photographs collected from the National Air Photo Library.

1. A16753_110	2. A16753_111
3. A16753_112	4. A16753_113
5. A16753_114	6. A16754_100
7. A16754_101	8. A16754_102
9. A16754_103	10. A16754_104
11. A16754_105	12. A16755_115
13. A16755_116	14. A16755_117
15. A16755_117	16. A16755_118
17. A16755_119	18. A16836_029
19. A16836_030	20. A16836_031
21. A16836_032	22. A16836_033
23. A16836_034	24. A16836_035
25. A16836_125	26. A16838_126
27. A16836_127	28. A16836_128
29. A16836_129	30. A16836_130
31. A16836_131	32. A16840_026
33. A16840_027	34. A16840_028
35. A16840_029	36. A16840_030
37. A16840_031	38. A16840_032
39. A16864_033	40. A16864_034
41. A16864_035	42. A16864_036
43. A16864_037	44. A16864_038

Chapter 4

RESULTS

In this chapter, I first present the area changes (Objective I) of Adams Icefield as a whole between 1948 and 2019, and then the changes of its individual ice masses (Baby, Trent, and Black Crown glaciers) and a nunatak between 1959 and 2019. These were computed using a combination of historical aerial photographs and contemporary high-resolution satellite imagery. I then present volume and mass changes of Adams Icefield (Objective II) through analysis of the 2001, 2012, and 2019 DEMs. Finally, I analyze thickness changes of Baby Glacier between 1959 and 2019 at the location of three 2014 GPR transects. As a result of the numerous datasets and methodologies used in this thesis, the results are presented in multiple formats such as percentage change, total change, and rate of change, in order to allow for a comparison of my results with those of other studies.

4.1 Objective I: Area Change Results

4.1.1 Area Change of Adams Icefield

Between 1948 and 2019, Adams Icefield decreased in area by 39.71%, with a reduction in ice cover from 3.63 km^2 in August 1948 to 2.11 km^2 in July 2019. This represents a decrease in area of 1.52 km^2 over the 71-year study period for the entire icefield, with the most substantial reductions occurring on the northern slope of Black Crown Glacier, the terminus of Baby Glacier, and the northwestern slope of Trent Glacier (Figures 4.1 & 4.2; Table 4.1). From 1948 to 1999 the decrease in ice cover for Adams Icefield as a whole was generally gradual (-0.0129 km^2 year^{-1}). Area losses accelerated after 2000 (-0.0486 km^2 year^{-1}), but rates slowed again between 2012 and

2019 (-0.0143 km^2 $year^{-1}$) (Figure 4.3A). The 1948 to 2019 linear trendline in Figure 4.3A (blue dotted line) illustrates an average ~0.0200 km^2 $year^{-1}$ decrease in area over the 71-year study period. To investigate the change in areal extent pre-and post-2000, linear trendlines were created for the periods 1948-1999 (red dotted line) and 2000-2019 (green dotted line) (Figure 4.3A). During the first period (1948-1999) Adams Icefield lost an absolute area of 0.6279 km^2, while it lost an absolute area of 0.9034 km^2 during the second period (2000-2019), for a total decrease of 1.52 km^2 between 1948 and 2019.

4.1.2 Area Change of Baby Glacier

Between 1959 and 2019, Baby Glacier decreased in area by 0.29 km^2 (1959 total area: 0.83 km^2; 2019 total area: 0.54 km^2), representing a reduction in ice cover of ~35% (Figure 4.3B & 4.4; Table 4.1) over the 60-year study period. Unlike the entirety of Adams Icefield, area change for Baby Glacier could only be calculated from 1959 to 2019, rather than 1948 to 2019, as Wolf Peak eclipsed the eastern extent of this niche glacier in the 1948 historical aerial photograph (Figure 3.3A).

The most significant retreat in extent of Baby Glacier occurred along the terminus in the lower ablation zone, where the margin of the glacier moved ~200 m northeast up the valley between Wolf and Black Crown peaks. Significant area reduction also occurred along the saddle (in the accumulation zone) which separates Baby Glacier and Black Crown Glacier. In 1959 the width of the saddle was ~590 m, while in 2019 the saddle was only ~235 m wide, which is a reduction of 355 m (60%) (Figure 4.1). This growing incision may result in Baby Glacier detaching from Adams Icefield in the future, which could result in a significant increase in the rate of area and mass loss due to the exposure of new low albedo bedrock adjacent to the glacier. Similar to

Adams Icefield, the decrease in area of Baby Glacier prior to the year 2000 was gradual (1959-1999: -0.004 km^2 $year^{-1}$), but post-2000 the decrease in area has occurred much more rapidly (2000-2019: -0.008 km^2 $year^{-1}$) (Figure 4.3B; blue line).

4.1.3 Area Change of Trent Glacier

Over the study period, Trent Glacier decreased in areal extent by 0.37 km^2 (1959 total area: 0.84 km^2; 2019 total area: 0.47 km^2), representing a 44% reduction, the largest of the three ice masses that comprise Adams Icefield (Figures 4.3 & 4.5; Table 4.1). Similar to Baby Glacier, the study period for Trent Glacier started in 1959, as Wolf Peak eclipsed nearly the entirety of the eastern perimeter of the glacier in 1948 (Figure 3.3A). Unlike Baby Glacier, Trent Glacier did not start rapidly decreasing in areal extent until around 2008 (Figure 4.3B; red line), with Trent Glacier having the smallest area (0.47 km^2) of all three ice masses by summer 2019.

The most significant decrease in area for Trent Glacier occurred around the terminus, where the glacier margin moved ~250 m up the valley, ~50 m more than the terminus of Baby Glacier. As well, a large portion of glacial ice along the northwestern extent of Trent Glacier disappeared entirely between 1948 and 1999. This wing of ice extended up the bedrock valley towards an unnamed mountain peak which separates Trent Glacier from Crusoe Glacier. It reduced in length by ~114 m between 1948 and 1979, and reduced by a further ~95 m between 1979 and 2019. A small remnant of the ice wing can still be seen in the 2019 extent (Figure 4.5).

4.1.4 Area Change of Black Crown Glacier

Between 1959 and 2019, Black Crown Glacier decreased in area by 0.72 km^2 (1959 total area: 1.82 km^2; 2019 total area: 1.10 km^2), representing a 40% reduction (Figures 4.3 & 4.6; Table 4.1). Black Crown Glacier experienced a small and short decrease in area around the year 2000, but then little change until the year 2006, when a rapid rate of decrease in area of -0.063 km^2 per year occurred until the year 2012 (Figure 4.3B; green line). This follows a similar pattern to that of Baby and Trent glaciers.

Black Crown Glacier underwent significant areal change of its northeastern and eastern extents, in close proximity to Baby Glacier. In 1959, a large glacial lobe extended east from Black Crown Glacier, which has now receded by 552 m. The reduction of this lobe was complex as between 2006 and 2007 a 0.025 km^2 lobe detached from the main body of Black Crown Glacier. This detached lobe further decreased in area (2008 total area: 0.009 km^2; 2009 total area: 0.005 km^2), until it disappeared entirely sometime between summer 2009 and summer 2012.

4.1.5 Area Change of Adams Icefield Nunatak

Over the period 1959-2019 the area of Adams Icefield nunatak, located within Black Crown Glacier, increased by ~296 times between 1959 (0.0001 km^2) and 2019 (0.0296 km^2) (Figures 4.1 & 4.7; Table 4.1). The majority of this nunatak area change has occurred since the year 1999, at an average rate of 0.0004 km^2 year^{-1}. The 1979 Landsat-1 satellite scene did not have a high enough resolution to accurately delineate the extent and area of the nunatak, so the next available outline was from 1999. Similar to the area change of Adams Icefield, prior to the year 2000 the increase in area was small, but post-2000 the area of the nunatak increased significantly as the glacial ice around it reduced in thickness and volume.

4.2 Objective II: Thickness, Volume, and Mass Change Results

Absolute and yearly mass and volume changes were quantified for Adams Icefield from 2001 to 2019, while cross-sectional thickness changes of Baby Glacier were determined from 1959 to 2019. An assessment of the accuracy of the DEMs is provided first, before presentation of the change results.

4.2.1 Error Assessment of Digital Elevation Models

In order to assess the accuracy of the DEMs, apparent changes in elevation over stable terrain (bedrock) surrounding Adams Icefield were calculated (Figure 4.8). The primary assumption of this method is that the bedrock did not significantly change in elevation over the study period (2001-2019), with the difference in bedrock elevation between two DEMs providing an estimate of their accuracy. In this study, the systematic bias (mean and standard deviation) was only calculated on bedrock with slope angles ranging from 0-30°, as small positional errors can result in large vertical errors on terrain with steeper slopes (Figure 4.8D) (Nuth and Kaab, 2011). The systematic bias (m) was then subtracted or added to elevation change values over ice-covered areas to account for this error. The systematic bias between the 2001 and 2012 DEMs was -1.277 m, while the systematic bias between the 2012 and 2019 DEMs was 1.106 m. As mentioned above, the random error is estimated from the standard deviation of the stable terrain differences. The random error between the 2001 and 2012 DEMs was 7.421 m, and 1.394 m between the 2012 and 2019 DEMs.

The accuracy of DEMs was also verified by assessing internal consistency in elevation change patterns based on two factors: (a) elevation changes over ice should be much greater than over bedrock, and (b) a gradient in elevation changes is frequently found on glaciers, with lower elevation ice experiencing greater change in elevation than ice at higher elevation (Hagen *et al.*, 2003; Paul and Haeberli, 2008).

When comparing the stable terrain between the 1959 and 2019 DEMs (Figure 4.8A), it is clear that there were numerous erroneous values as the elevation change values ranged from -150 to 80 m. High errors with the 1959 DEM can be primarily traced back to a lack of GCPs. A total of ten GCPs were used to create the 2019 DEM, which provided a solid means for orienting and relating the air photos to a ground coordinate system, improving its spatial accuracy. However, only three GCPs could be used when creating the 1959 DEM, resulting in a lower spatial accuracy. There was also poor internal inconsistency in the DEM of difference, as apparent elevation changes over glaciers were similar to those over bedrock, and no distinctive elevation change patterns across the glaciers (Fig. 4.8A). When combined with the large apparent elevation changes over bedrock, it was concluded that the errors associated with the 1959 DEM were far too great, so it could not be used for calculating volume and mass changes of Adams Icefield.

In contrast, the relatively small elevation change values (-1.277 m) over bedrock for the 2001-2012 DoD (Figure 4.8B) and 2012-2019 DoD (Figure 4.8C), along with internally consistent changes over ice, indicated that the 2001, 2012, and 2019 DEMs were suitable for use. The systematic bias of the 2001-2012 DoD over bedrock was -1.277 m, with a standard deviation of 7.421 m. Therefore, 1.277 m was added to the entire ice-covered area for the 2001-2012 DoD, before the volume and mass calculations were performed. The systematic bias associated with the 2012-2019 DoD was 1.106 m, with a standard deviation of 1.394 m. As a result, 1.106 m was subtracted from the entire ice-covered area before volume and mass calculations were completed.

4.2.2 Volume and Mass Changes of Adams Icefield Between 2001 and 2012

In order to quantify the volume and mass changes of Adams Icefield between 2001 and 2012, the August 19, 2001 ASTER DEM was subtracted from the July 2, 2012 ArcticDEM. This calculation indicates that the icefield lost a total of 13.4 million tonnes of ice (volume: -15,802,316 m^3), which represents an average thickness change of -0.48 m w.e. $year^{-1}$ over the eleven-year study period (Figure 4.9). This was computed using the mean area between 2001 and 2012.

The greatest thickness changes occurred at the termini of all three glaciers (Baby, Trent, and Black Crown glaciers), with the most significant being at Trent Glacier (Figure 4.9C). Volume loss was correlated with elevation, as regions with higher elevations lost less ice than at lower elevations. For example, thickness loss at the terminus of Trent Glacier ranged from -20 to -74.18 m (Fig. 4.9C; deep red and orange colouring), while thickness loss at the saddle of Trent Glacier ranged from -1.99 to 4 m (Fig. 4.9C; light yellow colouring). Similarly, volume losses tended to be higher along the margins of each glacier, where the ice was in close proximity to low albedo, snow-free bedrock, which warms rapidly in the spring and summer and accelerates the melting of nearby ice.

Over the period 2001-2012, Adams Icefield lost a total of -2 to -6.74 m $year^{-1}$ at the termini of Trent and Baby glaciers, while higher elevation regions such as the saddle of Baby Glacier lost 0 to -0.99 m $year^{-1}$ (Figure 4.9D). Total average thickness change for Adams Icefield between 2001 and 2012 was -5.28 m w.e.

4.2.3 Volume and Mass Changes of Adams Icefield Between 2012 and 2019

Between 2012 and 2019 Adams Icefield lost a total of 6.2 million tonnes of ice (volume: -6,197,024 m^3), which represents an average thickness changes of -0.35 m w.e. $year^{-1}$ over the seven-year period (Figure 4.10). These values were calculated by subtracting the July 2, 2012 ArcticDEM from the July 10, 2019 SfM DEM using the mean area between 2012 and 2019.

Similar to the 2001-2012 DoD, the greatest loss of thickness (m) is located at the termini of all three glaciers, with Baby Glacier illustrating the largest thickness change ranging from -10 to -27.76 m (Figure 4.10C; deep red and orange colouring). Overall, lower elevations on the glaciers, particularly close to their termini, experienced larger change than at higher elevations. As well, over the course of the study period (2012-2019), Adams Icefield loss -2 to -3.97 m year^{-1} in high volume loss regions such as at the margin of the glaciers and ice at low elevations (Figure 4.10D).

4.2.4 Thickness Changes of Baby Glacier

Based on data from the spring 2014 GPR survey (Figures 4.11 & 4.12), greater ice thickness change on Baby Glacier occurred at the ablation zone transect (Transect 00) than at the mid-glacier transect (Transect 01), or the accumulation zone transect (Transect 02). Overall, the ablation zone (Transect 00) thickness change rate between 2001 and 2019 was -1.39 m year^{-1}, with a total thickness change of ~25 m. Broken down by period, the thickness change rate between 2001 and 2012 was -1.82 m year^{-1} for a total thickness change of ~20 m. Between 2012 and 2019 the thickness change rate was -0.71 m year^{-1} for a total thickness change of ~5 m.

Between 2001 and 2019, the thickness change rate of Transect 01 (mid-glacier) was -0.83 m yr^{-1} (total thickness change: ~15 m). Transect 01 showed a similar pattern to Transect 00, as the thickness change rate between 2001 and 2012 was -0.91 m year^{-1} (total thickness change of ~10 m), and -0.71 m year^{-1} between 2012 and 2019 (total thickness change of ~5 m).

The thickness change rate for the accumulation zone transect (Transect 02) between 2001 and 2019 was -0.56 m yr^{-1} (total thickness change: ~10m). Similar to Transects 00 and 01, Transect 02 has a greater thickness change rate between 2001 and 2012 (-0.64 m yr^{-1}; total thickness change: ~7 m) than it did between 2012 and 2019 (-0.43 m year^{-1}; total thickness change: ~3 m). These results are consistent with both the area and mass change measurements, as the rate of change was greatest between 2001-2012 and decreased in intensity between 2012-2019.

Since an accurate 1959 DEM does not exist for Adams Icefield, it is difficult to interpret what the surface of Baby Glacier looked like at that time. As a result, thickness change measurements were interpreted based solely on the elevation of the 1959 margins of Baby Glacier where they intersected the 2019 DEM (Figure 4.12). Based on the 1959 margin elevation measurements the absolute thickness change between 1959 and 2019 for Transect 02 was ~37 m, which represents a thickness change rate of -0.62 m year^{-1}. The absolute thickness change between 1959 and 2019 for Transect 01 was ~70 m, which represents a thickness change rate of -1.17 m year^{-1}, while the absolute thickness change over the same period at the ablation zone transect was -0.83 m year^{-1} (absolute thickness change of ~50 m). Based on the 2019 DEM, the elevation at which the 1959 extent crossed at the accumulation zone transect was between 1185 m (NW margin) and 1119 m (NE margin) a.s.l. The 1959 margin of the mid-glacier transect was between 1031 m (NW margin) and 1093 m (NE margin) a.s.l. and lastly, the 1959 margin of Baby Glacier at the ablation zone transect sat at an elevation ranging between 994 m (NW margin) and 893 m (NE margin) a.s.l.

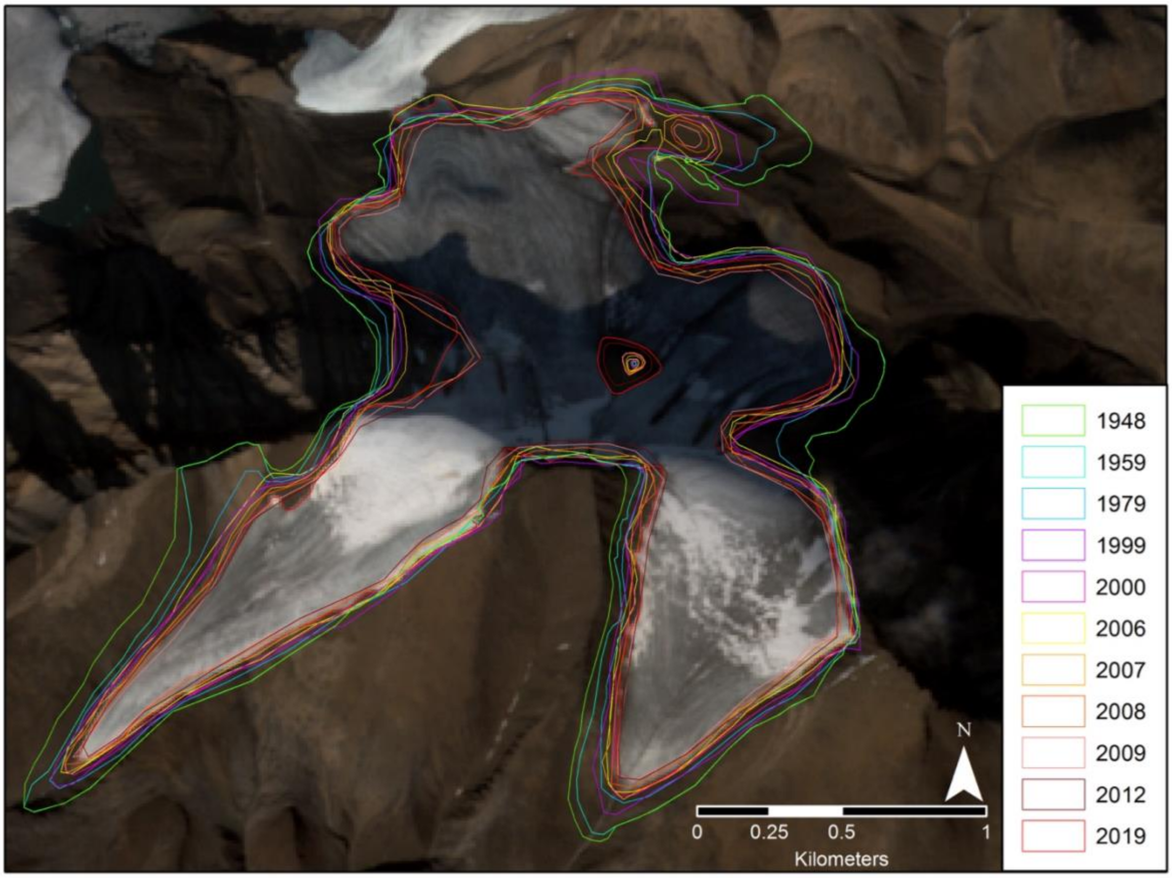

Figure 4.1. Change in areal extent of Adams Icefield between 1948 and 2019. Base Image: Sentinel-2A (July 4, 2019).

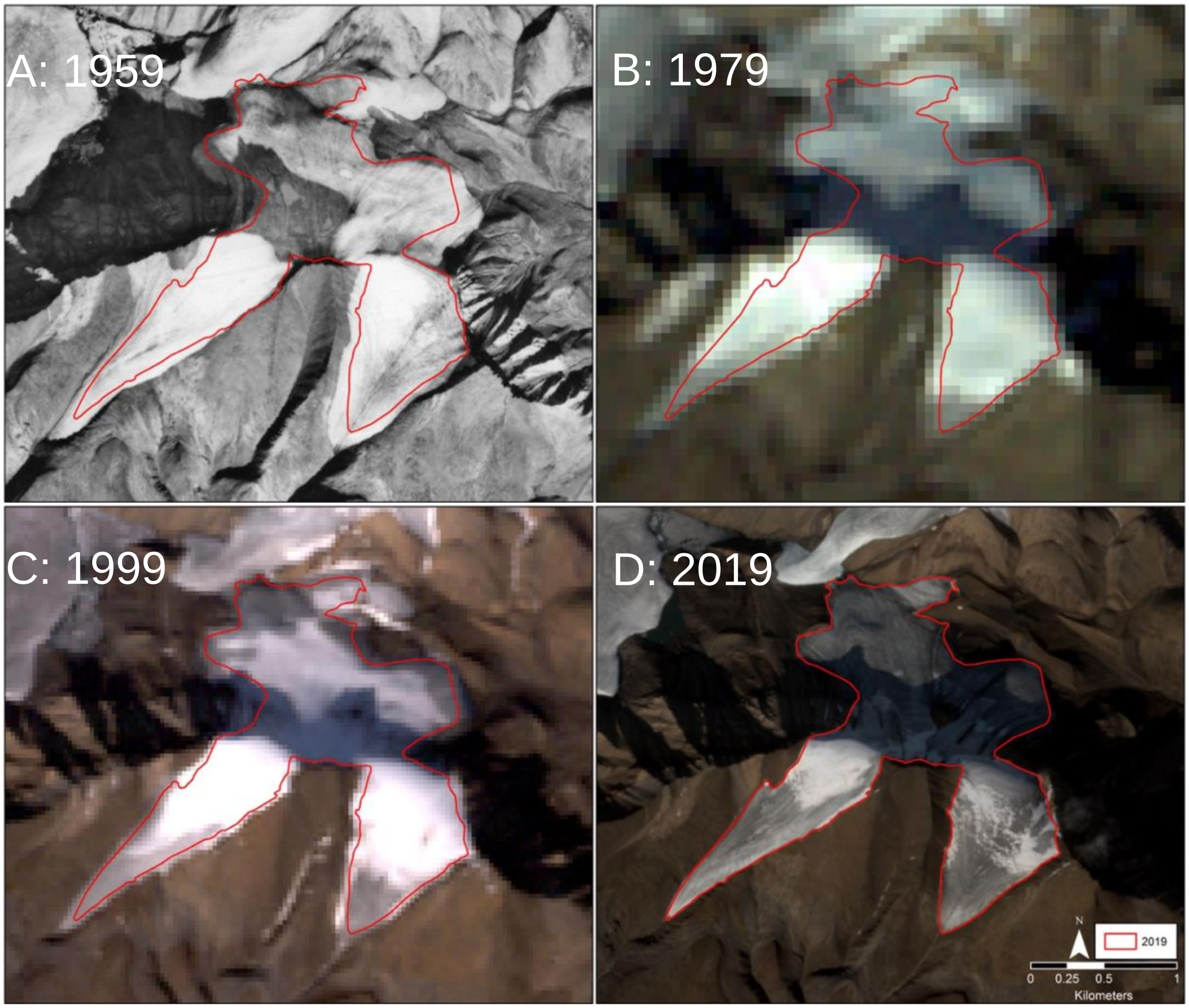

Figure 4.2. Imagery of Adams Icefield illustrating ice cover change from 1959 to 2019. A: Historical aerial photograph (A16836_030), July 28, 1959; B: Landsat-1, July 30, 1979; C: Landsat-7, July 25, 1999; D: Sentinel-2A, July 4, 2019. Red outline illustrates the 2019 icefield extent.

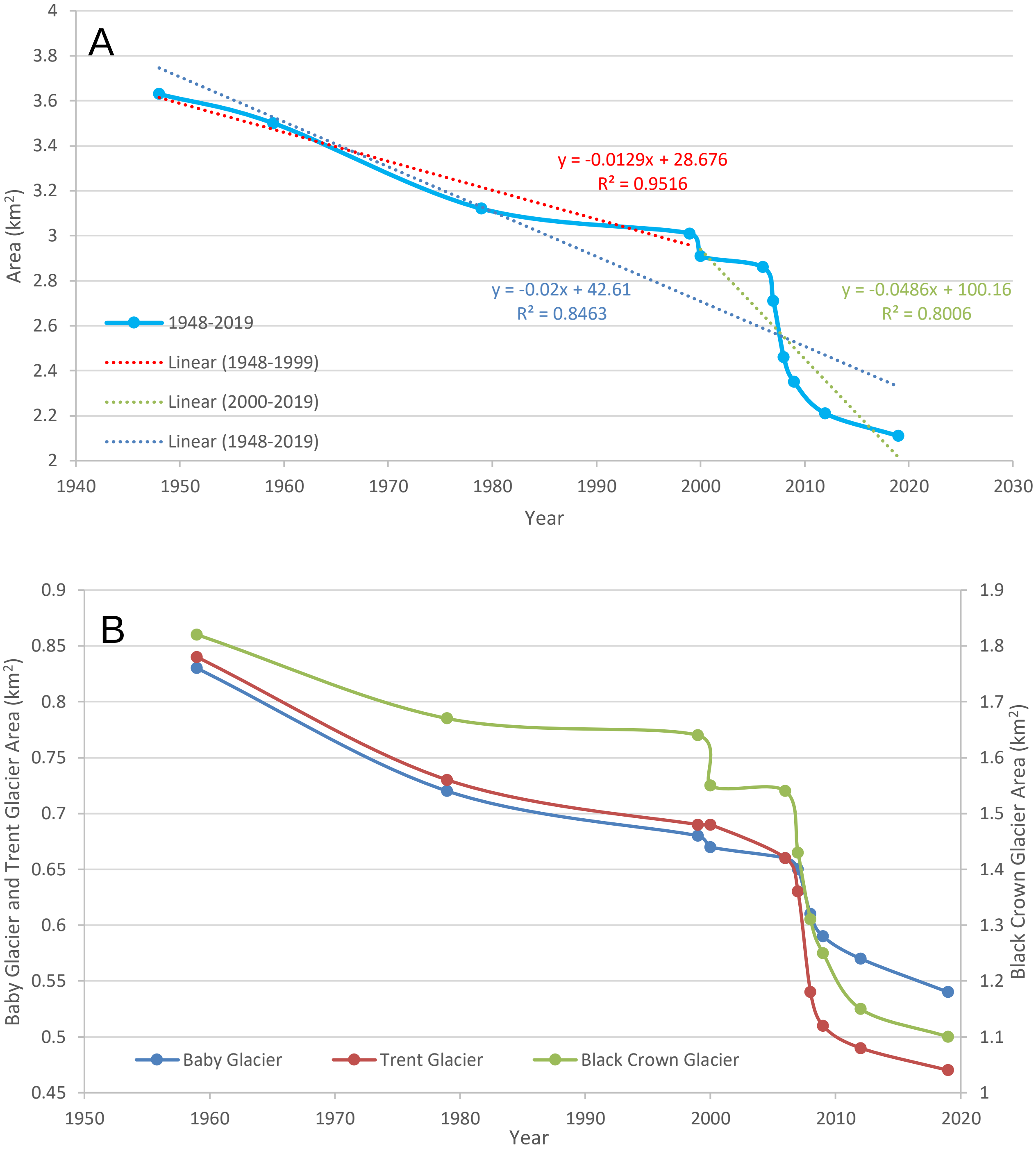

Figure 4.3. A: Change in areal extent (km²) for Adams Icefield from 1948 to 2019; red best fit line represents 1948 to 1999, green best fit line represents 2000 to 2019. B: Change in areal extent (km²) for Baby, Trent, and Black Crown glaciers from 1959 to 2019.

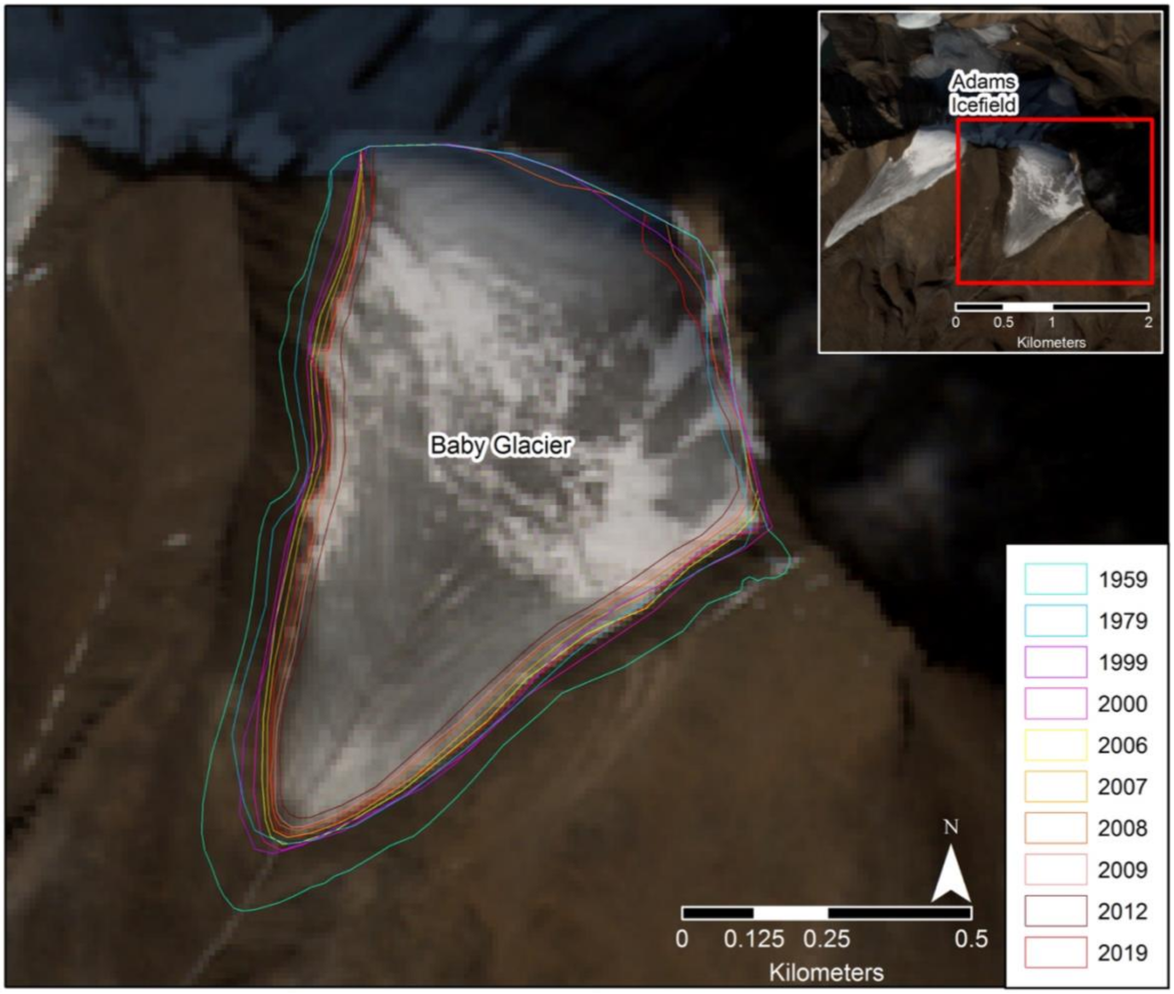

Figure 4.4. Change in extent of Baby Glacier between 1959 and 2019; inset map illustrates the location of Baby Glacier within Adams Icefield. Base Image: Sentinel-2A (July 4, 2019).

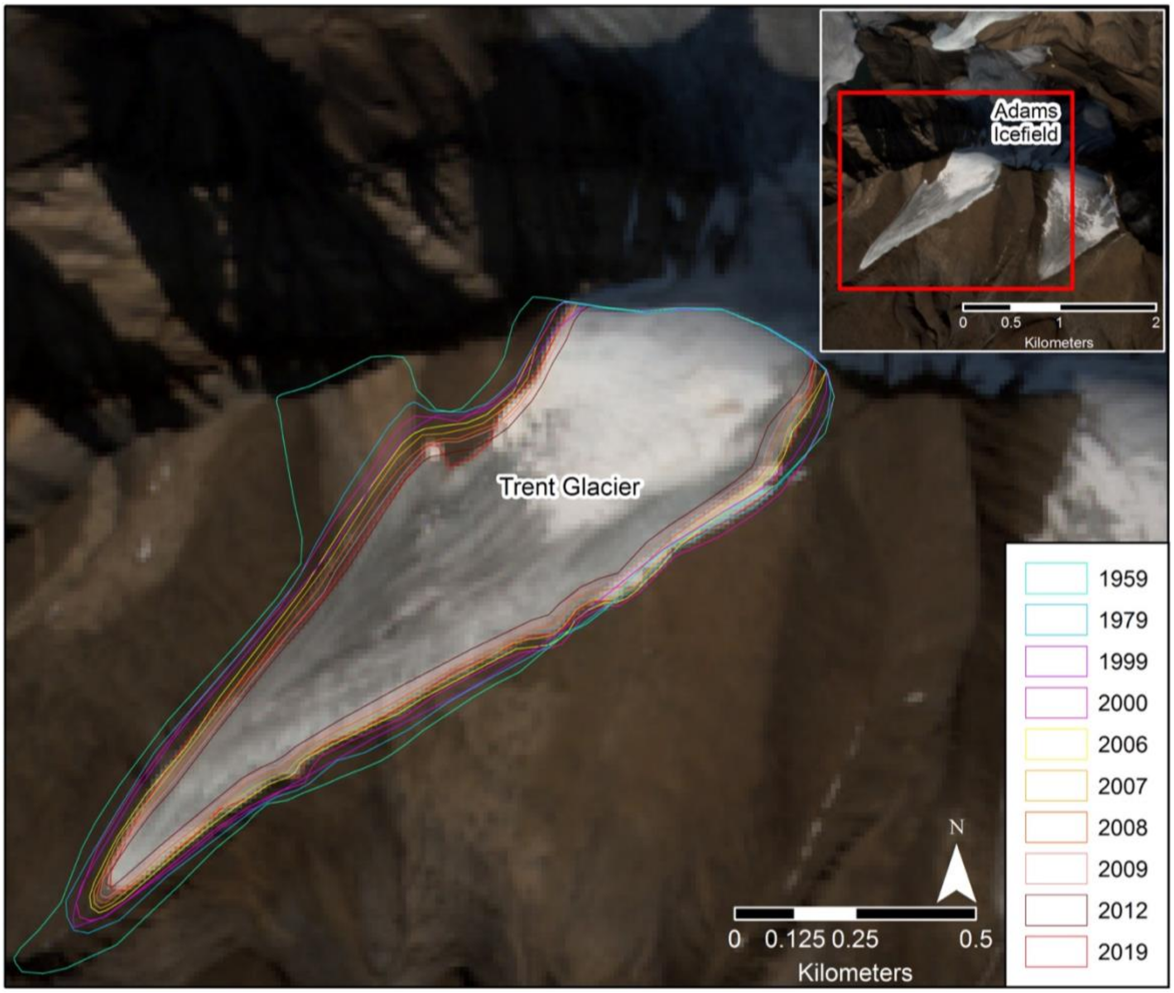

Figure 4.5. Change in extent of Trent Glacier between 1959 and 2019; inset map illustrates the location of Trent Glacier within Adams Icefield. Base Image: Sentinel-2A (July 4, 2019).

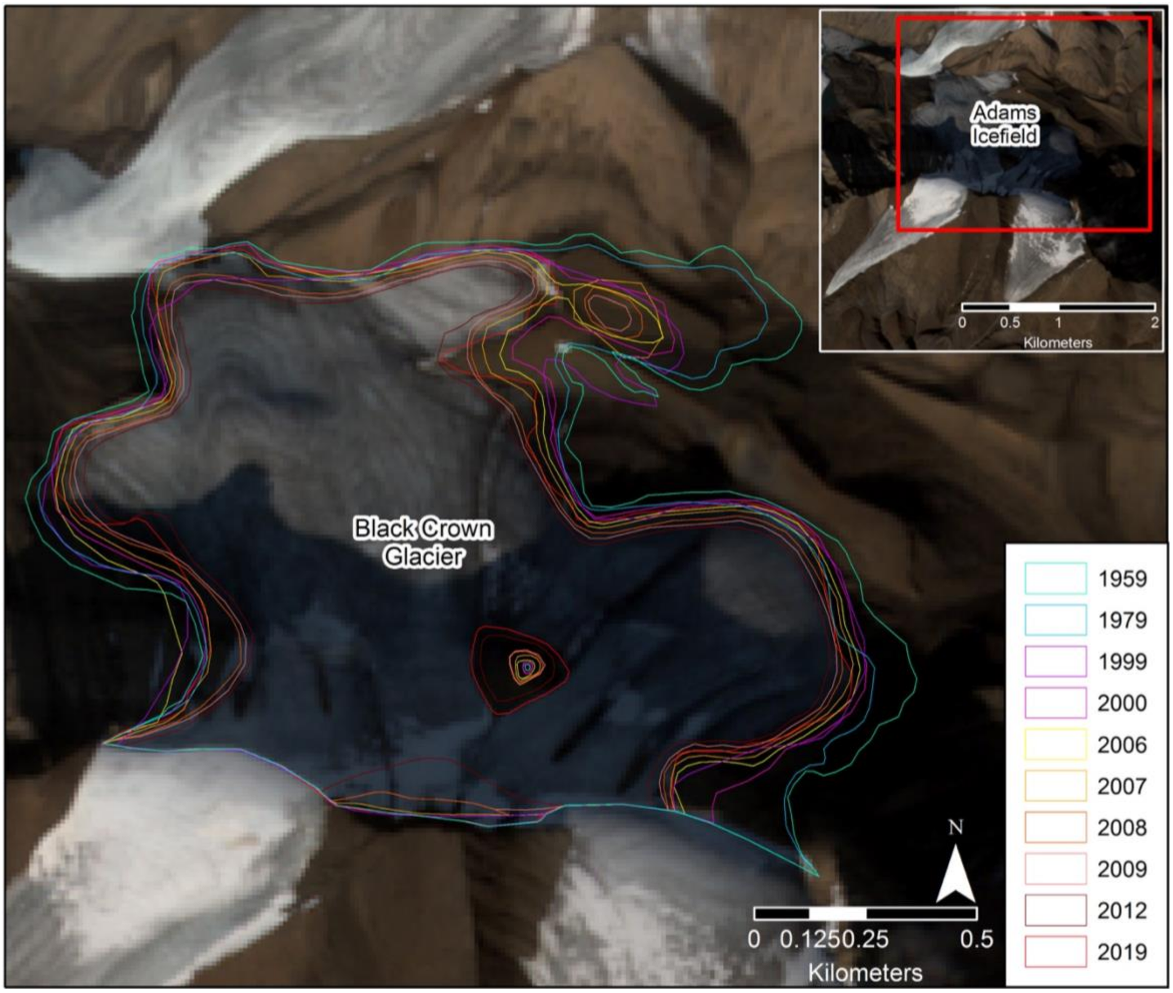

Figure 4.6. Change in extent of Black Crown Glacier between 1959 and 2019; inset map illustrates the location of Black Crown Glacier within Adams Icefield. Base Image: Sentinel-2A (July 4, 2019).

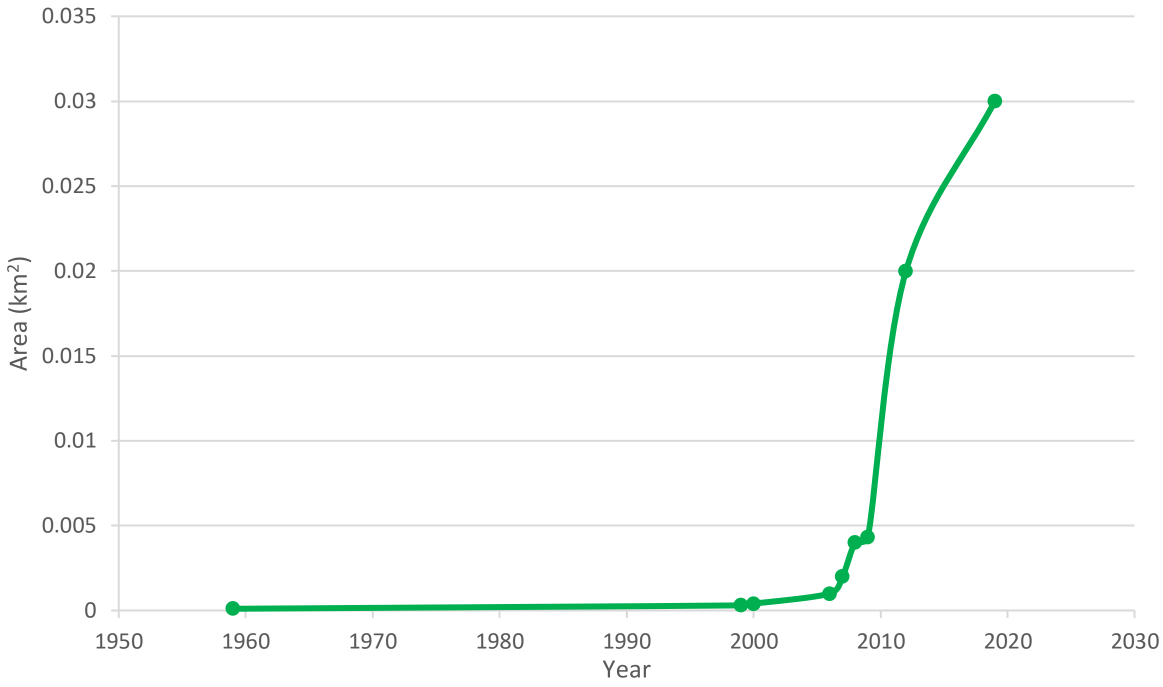

Figure 4.3. Change in areal extent (km^2) for the Adams Icefield nunatak from 1959 to 2019.

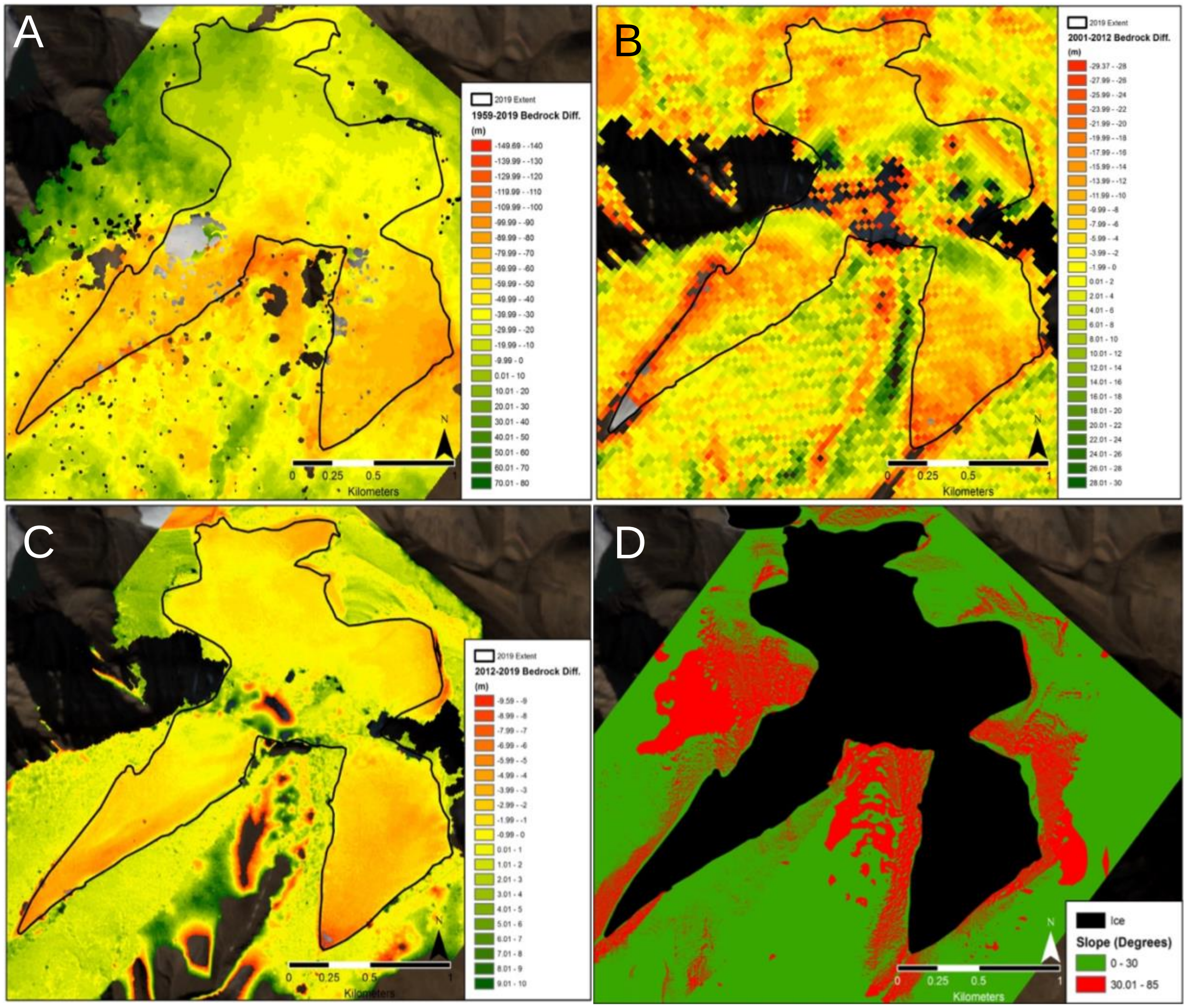

Figure 4.8. A: DoD for stable terrain from 1959 to 2019 of Adams Icefield; B: 2001-2012; C: 2012-2019; D: Stable terrain surrounding Adams Icefield based on 2019 DEM. Base Image: Sentinel-2A (July 4, 2019).

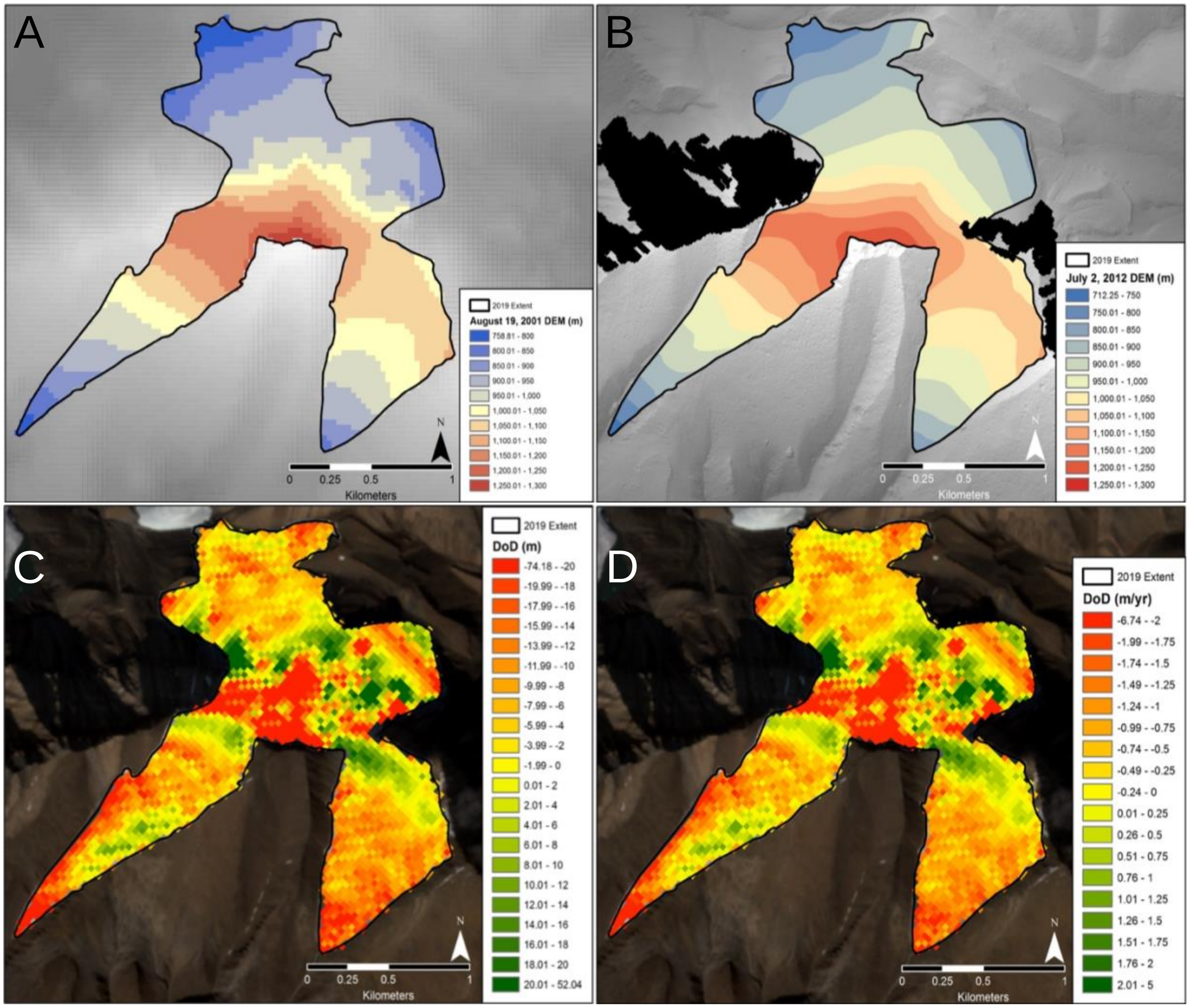

Figure 4.9. A: August 19, 2001 ASTER DEM of Adams Icefield; B: July 2, 2012 strip ArcticDEM of Adams Icefield; C: Absolute DEM of Difference (m; 2001-2012) of Adams Icefield; D: Annual DEM of Difference (m year^{-1}; 2001-2012) of Adams Icefield. Base Image: Sentinel-2A (July 4, 2019).

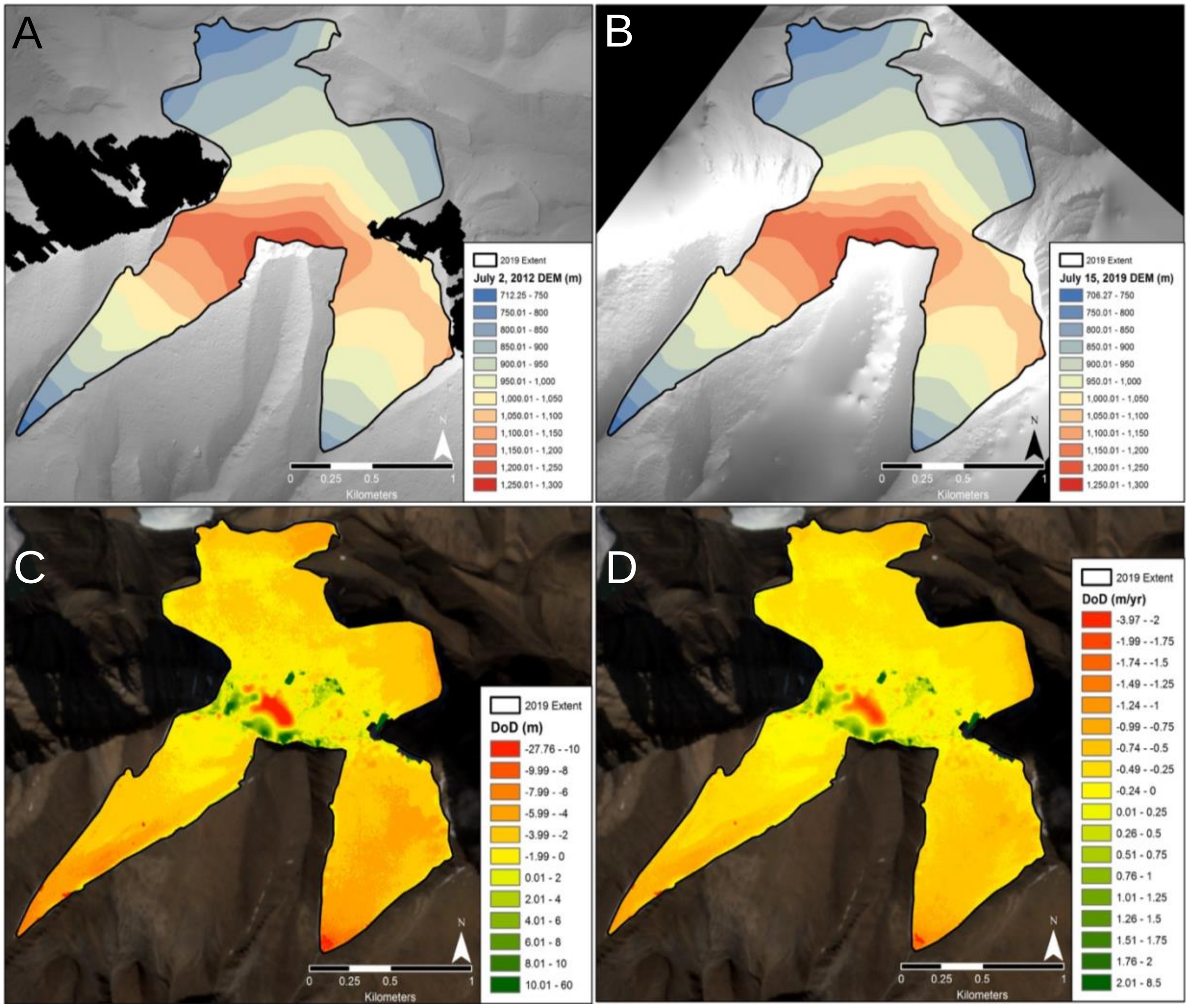

Figure 4.10. A: July 2, 2012 ArcticDEM of Adams Icefield; B: July 10, 2019 SfM DEM of Adams Icefield; C: Absolute DEM of Difference (m; 2012-2019) of Adams Icefield; D: Annual DEM of Difference (m year^{-1}; 2012-2019) of Adams Icefield. Base Image: Sentinel-2A (July 4, 2019).

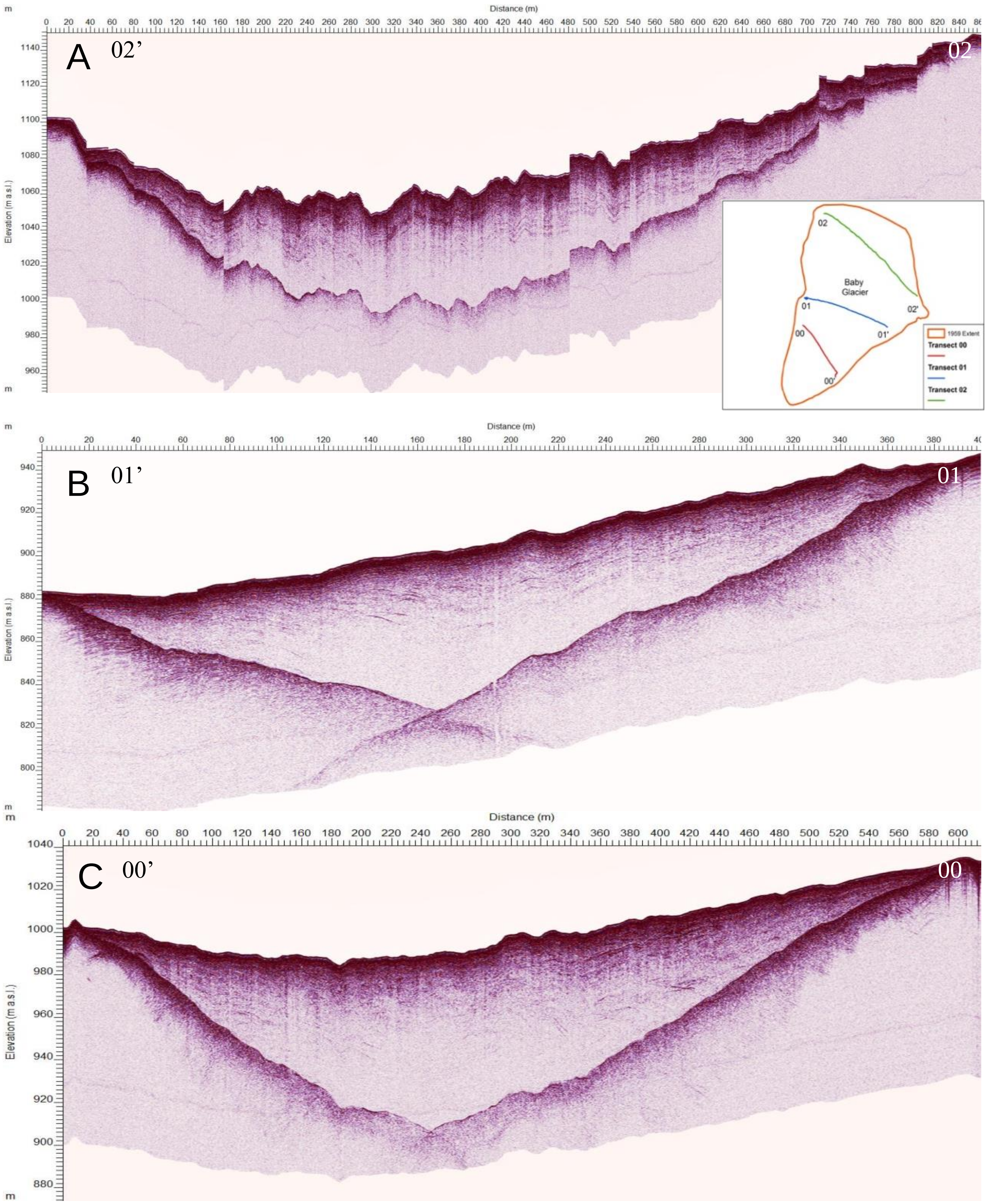

Figure 4.11. 2014 250 MHz topographically corrected GPR transects along Baby Glacier showing a maximum ice thickness of ~100 m. A: Transect 02; B: Transect 01 ; Transect 00. Inset map illustrates the location and orientation of each transect as well as the 1959 extent of Baby Glacier.

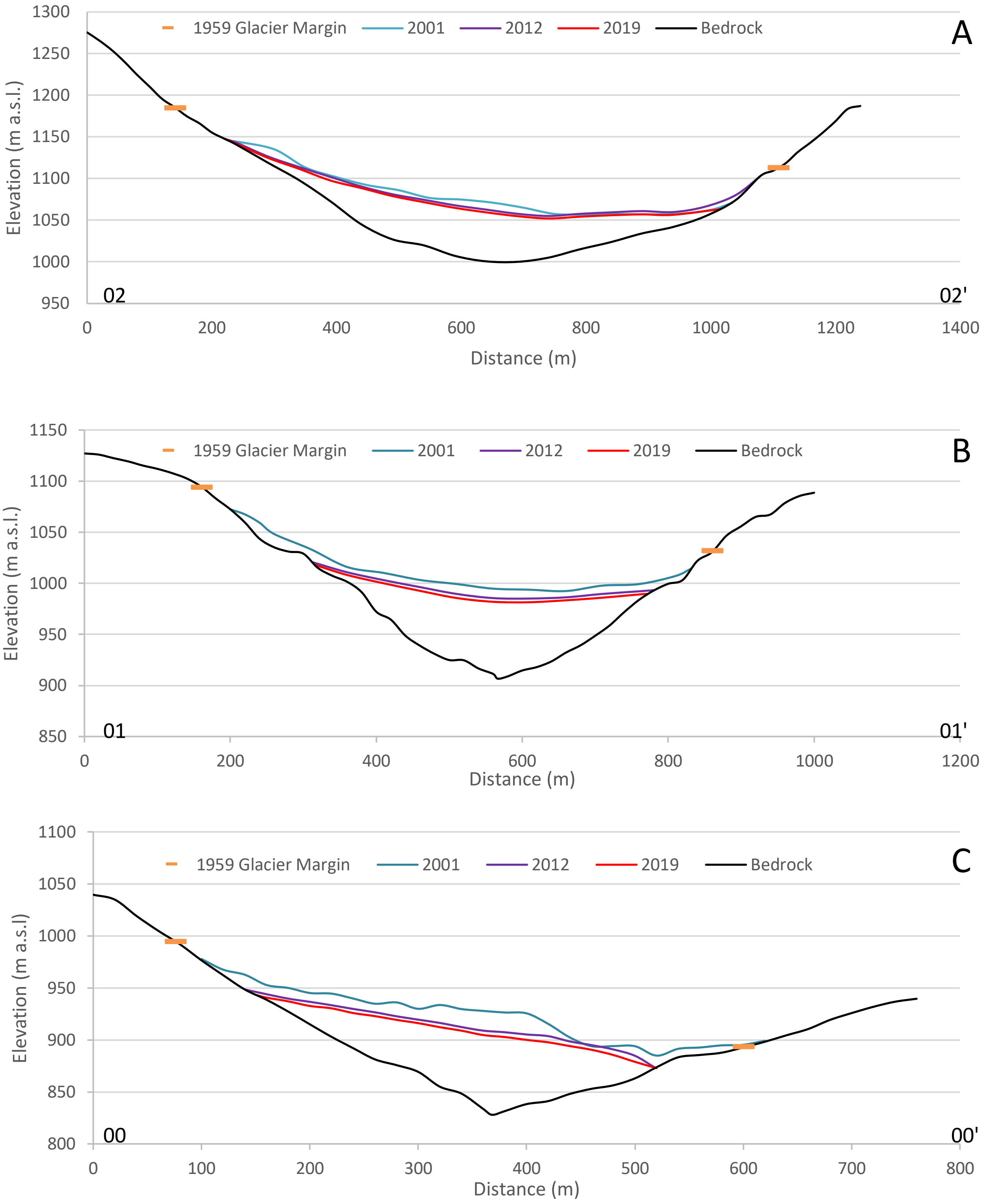

Figure 4.12. Cross-sectional thickness changes of Baby Glacier from 1959-2019. A: Cross-section 02 (Accumulation zone); B: 01 (Mid-glacier); and C: Cross-section 00 (ablation zone). 02 to 02'; 01 to 01'; and 00 to 00', signifies a NW-SE orientation for all transects; inset map on Figure 4.11C.

Table 4.1. Change in area through time for Adams Icefield and the individual glaciers and nunatak that comprise it.

Year	Adams Icefield (km^2)	Percentage of 1948 (%)	Rate (km^2 $year^{-1}$)	Baby Glacier (km^2)	Trent Glacier (km^2)	Black Crown Glacier (km^2)	Nunatak (km^2)
1948[1]	3.63	100	-	-	-	-	-
1959[1]	3.50	96	0.012	0.83	0.84	1.82	0.0001
1979[2]	3.12	86	0.019	0.72	0.73	1.67	-
1999[2]	3.01	83	0.005	0.68	0.69	1.64	0.0004
2000[2]	2.91	80	0.100	0.67	0.69	1.55	0.0004
2006[2]	2.86	79	0.008	0.66	0.66	1.54	0.0013
2007[2]	2.71	75	0.150	0.65	0.63	1.43	0.0025
2008[2]	2.46	68	0.250	0.61	0.54	1.31	0.0038
2009[2]	2.35	65	0.110	0.59	0.51	1.25	0.0043
2012[2]	2.21	61	0.047	0.57	0.49	1.15	0.0184
2019[3]	2.11	58	0.014	0.54	0.47	1.10	0.0296

[1] Aerial photograph. [2] Landsat scene. [3] Sentinel scene.

Table 4.2. Change in mass and volume for Adams Icefield between 2001-2012 and 2012-2019.

Period	**Volume Change (m^3)**	**Mass Change (m w.e.)**	**Mass Change Annual Rate (m w.e. $year^{-1}$)**	**Total Mass Change (Mt)**	**Thickness Change Error (m)**
2001-2012	-15,802,316	-5.29	-0.48	-13.4	±7.421
2012-2019	-6,197,024	-2.44	-0.35	-6.2	±1.394
Total:	-21,999,340	-7.73	-	-19.6	-

Chapter 5

DISCUSSION

In this chapter, I discuss the implications of the results for area, thickness, and volume changes of Adams Icefield and its individual glaciers between 1948/1959 and 2019, and relate them to previous studies, as well as examine the future fate of this icefield (Objective III). From the results, it is clear that the small glaciers studied have experienced significant losses since the mid-twentieth century, with two main trends standing out among the observations: (1) rapid wastage has increased dramatically since the beginning of the twenty-first century; (2) the future fate of low-lying, small glaciers is likely short as area and mass changes are strongly negative. In the following analysis, I begin by comparing my results against those of other glaciers and icefields within the QEI. I then examine the relationship between area changes of Baby, Trent, and Black Crown glaciers with changes in the equilibrium line altitude (ELA) and accumulation area ratio (AAR). Finally, in order to gain a better understanding of the future fate of these small ice masses, I examine their trends in area, mass, and volume changes to predict when their disappearance is likely to occur.

5.1 Climatological Changes in the QEI

Summer air temperatures are considered the leading control on glacier mass balance, and subsequent changes in area and volume (Sharp *et al.*, 2011). According to Mortimer (2017), who completed a climate analysis of data from both the Eureka and Resolute Bay weather stations, summer air temperatures between 2005 and 2015 were 1.2°C higher than the 1948 to 2015 mean.

As well, the warmest pentads for both weather stations occurred from 2005-2009 and 2010-2014, both after the start of the twenty-first century. Mortimer (2017) also noted that the three warmest summers on record at Eureka since 1948 were 2009, 2011, and 2012. The three warmest summers of the last 68 years at Resolute Bay were 2007, 2011, and 2012, with 2013 being the coldest summer at Eureka and the eleventh at Resolute Bay. In relation to my study period (1948 to 2019), Mortimer (2017) noted that the QEI experienced lower than normal mean air temperatures between the mid-1960's and mid-1990's, in comparison to the 1948 to 2015 mean. However, from the late 1990's to 2015 a consistent increase in mean annual air temperature occurred, with the exception of 2013.

White and Copland (2018) also completed an analysis of temperature changes across Northern Ellesmere Island (~400 km to the northeast of Axel Heiberg Island) from NCEP/NCAR climate reanalysis. This analysis suggested that mean annual surface air temperatures increased by 3.6°C (0.5°C decade^{-1}) between 1948 and 2016, with temperatures increasing much more rapidly during the period 1995 to 2016 (0.78°C decade^{-1}) than the 1948 to 1994 mean (0.12°C decade^{-1}). They also found that 16 out of 20 of the warmest years since 1946 have occurred since the year 2000, with every summer since 2000 exceeding the long-term mean by 0.6°C to 2.7°C.

Canada's Climate Change Report (CCCR, 2019) made it clear that Canadian High Arctic glaciers and ice caps have thinned significantly over the past three decades due to increasing surface air temperatures. This observation aligns with the results from my study, particularly in relation to the connection between increases in warming over the study period and increasing rates of area loss towards the present day. For Adams Icefield as a whole, the period 1948 to 1999 saw a mean decrease in area of 0.0129 km^2 year^{-1}, compared to an almost quadrupling in the rate of area loss to 0.0486 km^2 year^{-1} over the period 2000 to 2019.

5.2 Regional Glacier Change

To place the findings of this study in context, it is useful to compare the changes measured at Adams Icefield against those measured at other glaciers and ice caps across the QEI, with a particular focus on small ice masses.

5.2.1 Glacier Area Changes within the QEI

Based on the analysis presented in Section 4.1, Adams Icefield decreased in area by 39.71% between 1948-2019, which represents a mean loss of 5.67% decade^{-1}. Each individual ice mass within Adams Icefield showed similar results over the period 1959-2019, with Baby Glacier decreasing in area by 35% (-5.83% decade^{-1}), Trent Glacier by 44% (-7.33% decade^{-1}), and Black Crown Glacier by (-6.66% decade^{-1}).

Previous studies in the QEI have established that glaciers which experience the highest rates of area loss are typically land-terminating with areas of less than ~1 km^2 (Thomson *et al.*, 2011; Sharp *et al.*, 2014; Serreze *et al.*, 2017; White and Copland, 2018). For example, White and Copland (2018) found that glaciers <1 km^2 in area (352 glaciers) on Northern Ellesmere Island decreased in area by an average of 30.4% decade^{-1} between 1999 and 2015. In contrast, glaciers in the next size category of 1-5 km^2 (548 glaciers) showed an average reduction in ice cover of ~14% decade^{-1} between 1999 and 2015. In 1999, Adams Icefield was 3.01 km^2 in area, and decreased in area by 14.95% decade^{-1} between 1999 and 2019, which is in close agreement with the Northern Ellesmere area loss rates.

The study of Sharp *et al.*, (2014), which analyzed glacier area change between ~1960 and ~2000 on Northern Ellesmere Island, also found substantial losses, although the rates of change were lower than those reported by White and Copland (2018). Glaciers and ice caps that were <1 km^2 experienced a decrease in area of 29.2% (7.3% decade^{-1}) between ~1960 and ~2000, with a decrease of 25.6% (6.4% decade^{-1}) for glaciers ranging in size from 1-5 km^2. Sharp *et al.* (2014) also analyzed percent area change for glaciers on Axel Heiberg Island (where Adams Icefield is located) between ~1960 and ~2000. For the glacier class size of <1 km^2, the mean change in area was -34.8% (-8.7% decade^{-1}) based on 56 glaciers, while the mean change for the class size 1-5 km^2 was -17.1% (-4.27% decade^{-1}) based on 68 glaciers.

Thomson *et al.* (2011) presented similar results concerning glacier change on Axel Heiberg Island by comparing a 1959 glacier inventory (Ommanney, 1969) against the 2000 GLIMS inventory (https://www.glims.org/). Once again, they found that glaciers that experienced the greatest decrease in area were small in size and situated at low-lying elevations, with the complete disappearance of 90% of ice masses that were smaller than 0.2 km^2 between ~1959 and 2000. Thomson *et al.*, (2011) also reported that glaciers and ice caps <25 km^2 in size experienced significant retreat (on the order of 50-80%) over the 41-year study period. As well, it was discovered that small ice masses on the northern and western peninsulas of Axel Heiberg Island (Adams Icefield is located on the western peninsula) experienced a total area loss of 992.89 km^2 between 1959 and 2000, the most of any region, which is the result of a high frequency of small ice masses. Therefore, the authors concluded that observations of significant retreat coincided with regions with a high number of small glaciers that were situated at low elevations.

Over a similar time period (1959-2000), my findings show that Adams Icefield decreased in area by 16.84% (4.21% decade^{-1}), which is very close to the findings of Sharp *et al.*, (2014) for the 1-5 km^2 class size. However, Trent Glacier which saw the largest decrease in areal extent in my study for a glacier that falls in the class size of <1 km^2, decreased in area by 17.86% between 1959 and 2000 (-4.46% decade^{-1}). These findings are half of the mean decadal change rate of -8.7%

decade^{-1} for glaciers of this size reported by Sharp *et al*., (2014). Results from this study were also consistent with area losses reported by Sharp *et al*., (2014) through the delineation of ice extent through historical photography and satellite imagery for the Prince of Wales Icefield, Agassiz Ice Cap, Southern Ellesmere Island, and Devon Ice Cap. Ice masses that were <1 km^2 in size showed the greatest reduction within the entire QEI (Sharp *et al*., 2014).

In the most detailed study to date of small glacier changes in the QEI, Serreze *et al*. (2017) analyzed four ice caps (the St. Patrick's Bay ice caps and the Murray and Simmons ice caps) within the Hazen Plateau on Northeastern Ellesmere Island between 1959 and 2016. Their findings revealed that the two St. Patrick's Bay ice caps only contained 5% of their 1959 area in 2016 (1959: 10.42 km^2; 2016: 0.50 km^2). The ice caps also shrank considerably within a single year between summer 2015 and summer 2016, which was most likely the result of an unusually warm summer in 2015. In comparison to the St. Patrick's Bay ice caps, the Murray and Simmons ice caps contained 39% and 25% of their 1959 area in 2016. Serreze et al. (2017) attributed this smaller decrease in area to the higher mean elevations (200-300 m difference) of these ice masses than the St. Patrick's Bay ice caps, which would suggest cooler summer temperatures.

5.2.2 Glacier Mass and Volume Changes within the QEI

Based on the analysis presented in Section 4.2, Adams Icefield decreased in average thickness by 0.48 m w.e. year^{-1} (total volume: -15,802,316 m^3) between 2001-2012, and by 0.35 m w.e. yr^{-1} (total volume: -6,197,024 m^3) between 2012-2019. The study of Mortimer et al. (2018) reported that ice masses in the QEI underwent average thickness change of -0.5 m year^{-1} between 1995 and ~2014 at lower elevations near glacier termini, with lower rates of thickness change at higher elevations. These findings are similar to those of Abdalati *et al*. (2004), who reported that

that average mass loss in the northern CAA (specifically Axel Heiberg Island, Northern Ellesmere Island, Devon Island, and Meighen Island) was ~0.5 m w.e. yr^{-1} over the period 1995 to 2000 on glaciers and ice caps at lower elevations (below 1600 m a.s.l.).

Mass loss results from Sharp *et al*. (2011), who analyzed the glaciological mass balance of four monitored ice masses within the QEI (Meighen Ice Cap, White Glacier, Devon Ice Cap, and Melville South Ice Cap) between 1963 and 2009 found that mass loss increased significantly after the start of the twenty-first century. Between 38% and 58% of the total mass loss since 1963 occurred between the period 2000 and 2009, including 30-48% of the mass loss occurring between 2005 and 2009 (mean rate of glacier mass loss: -0.493 m w.e. yr^{-1}). Geodetic mass loss measurements between 2004 and 2009 determined from ICESat and GRACE measurements over the entire CAA by Gardner *et al*. (2011) illustrated similar results, with mass losses increasing from 31 ± 8 Gt yr^{-1} between 2004 and 2006 to 92 ± 12 Gt yr^{-1} between 2007 and 2009.

White Glacier, a medium-sized glacier situated ~5 km northeast of Adams Icefield, underwent a cumulative glaciological mass loss of ~12 m w.e. between 1960 and 2014, equivalent to an average rate of -0.23 m w.e. year^{-1} over the entire glacier (Thomson *et al*., 2017). Although different in size, Adams Icefield and White Glacier likely experienced similar climatological conditions. White Glacier ranges in elevation from 100-1800 m a.s.l. and is ~14 km long with an area of ~40 km, as a result this valley glacier is significantly larger than Adams Icefield (Thomson *et al*., 2017). In contrast, the elevation range of Adams Icefield (750 m to 1200 m a.s.l.) is far more limited than that of White Glacier and these two ice masses should only be compared at common elevations over similar time periods.

Measurements of the average change in surface elevation at White Glacier between 1960 and 2014 (54-years) at ~900 m a.s.l. (the same elevation as Transect 00) suggest that White Glacier thinned at an average rate of -0.44 m $year^{-1}$. Transect 01 on Baby Glacier sits at an elevation of ~1000 m a.s.l.; the average rate of thinning for White Glacier at this elevation was -0.37 m $year^{-1}$. Lastly, the average rate of thinning for White Glacier at the elevation of ~1050 m a.s.l. (the same elevation as Transect 02 on Baby Glacier) was -0.33 m $year^{-1}$ (Thomson *et al*., 2017). Overall, the average thinning rates of White Glacier are less than that of Baby Glacier (Transect 00: 1.39 m $year^{-1}$; Transect 01: -0.83 m $year^{-1}$; and Transect 02: -0.56 m $year^{-1}$), which can be attributed to the different time spans of the datasets between the two glaciers, and perhaps differences in surrounding physical characteristics (e.g., shading, aspect, longwave radiation inputs from surrounding bedrock). Baby Glacier's average thinning rates were determined between 2001 and 2019, an 18-year time span which occurred when mass loss had increased significantly within the QEI (after the year ~2000). White Glacier's average thinning rates were calculated over a 54-year time span (1960-2014). This includes thickness change measurements prior to the year 2000 when mass losses in the QEI were substantially lower than they were at the start of the twenty-first century, resulting in slightly lower average thinning rates.

5.3 Objective III: Future Fate of Adams Icefield

Since the year ~2000, Canada's QEI has experienced a rapid increase in glacier and ice cap mass losses, making the Canadian Arctic one of the largest contributors to eustatic sea level rise (Noel *et al*., 2018; Wouters *et al*., 2019). As discussed above, Adams Icefield lost ice cover at a rate of 0.0129 km^2 $year^{-1}$ during the period 1948-1999 ($r^2 = 0.9516$; $P < 0.01$), while between 2000-2019 it lost ice cover at a rate of 0.0486 km^2 $year^{-1}$ ($r^2 = 0.8006$; $P < 0.01$). Trendlines illustrating these losses are provided in Figure 5.1. If the area change rate of -0.02 km^2 $year^{-1}$ (mean over 1948-2019 period; blue trendline; $r^2 = 0.8463$; $P < 0.01$) is projected forward in time, then Adams Icefield will likely disappear over the next century, with the 2130's as a conservative estimate. However, if the current, and more rapid, area change rate of the 2000-2019 period (-0.05 km^2 $year^{-1}$; green trendline) is projected forward, then Adams Icefield will disappear entirely over the next few decades, with the early 2060's being a conservative estimate.

According to Figure 5.2, ~79.49% of Adam Icefield's remaining area exists at an elevation ranging from 850 to 1100 m a.s.l., with ~11.82% above 1100 m a.s.l. and 8.68% below 850 m a.s.l. As mentioned above, the Serreze *et al*. (2017) study found that ice caps occurring at lower elevations (the St. Patrick's Bay ice caps: 880-720 m a.s.l.) lost area at a significantly higher rate (5% of their 1959 area remaining) than the Murray and Simmons ice caps (39% and 25% of remaining of their 1959 area) that were found at higher elevations (1000-1100 m a.s.l.). Adams Icefield covers a similar elevation range to these ice masses, with more than one-third (35.48%) of its area ranging from 750 to 900 m a.s.l., a similar elevation as the St. Patrick's Bay ice caps, which suggests that a significant decrease in area will continue well into the twenty-first century.

To provide further insight into the historical and future changes of Adams Icefield, it is useful to measure how the snow line has changed over time because it can be used as an indication of the Equilibrium Line Altitude (ELA). The snowline was identified as the boundary between an ice-covered and snow-covered surface in later summer optical satellite imagery. Elevation values were derived from the 2012 ArcticDEM. In 1979, the mean elevation of the snowline was 894 m a.s.l. which increased to 1022 m a.s.l. for the year 2019 (Figure 5.3 and Table 5.1). This indicates that as time has progressed the ELA of the region has increased, resulting in a smaller accumulation zone and more ablation of Adams Icefield. The ELA reached its highest elevation in the year 2012 at 1057 m a.s.l., compared to 953 m a.s.l. in the year 2000. Even with a slight decrease in elevation over the past seven years, the ELA increased significantly (by ~130 m) over the past four decades, allowing for a larger region of glacier ice to be exposed by the end of each summer melt season.

Based on the ELA, the Accumulation Area Ratio (AAR) was computed for the years 1979, 2000, 2012, and 2019 of all three glaciers within Adams Icefield from late summer satellite imgery. This was calculated from the fraction of the glacier that occurred above the ELA compared to total area of each glacier for each particular year. Results indicate that as time has progressed, the accumulation zone has decreased for the majority of Adams Icefield (Table 5.1). In 1979, the AAR of Baby Glacier was 0.92, suggesting that most of this niche glacier was in the accumulation zone, while the 2019 AAR was 0.74. However, the 2012 AAR for Baby Glacier was 0.28 which indicates that less than one third of the glacier was in the accumulation zone that year. Trent Glacier's AAR showed a more consistent decrease in AAR over time, with a value of 0.90 in 1979, similar to Baby Glacier. Given that both glaciers are at similar elevations and size, these results are not surprising. The AAR continued to decrease to 0.78 in 2000, to 0.55 in 2012, with a light increase to 0.57 in 2019. The 2019 AAR suggest that just under two thirds of the area of Trent Glacier was within the accumulation zone. These results closely follow the area change results as Trent Glacier lost the most in ice cover (-44%) over the course of the study (1959-2019), which suggests that significantly less of the glacier is in the accumulation zone towards present day. Only two AAR values could be calculated for Black Crown Glacier, due to uncertainty with identifying the snowline for the years 1979 and 2012 due to shadowing. The 2000 AAR was 0.75, while the 2019 AAR was 0.44. These results suggest that the accumulation zone has decreased in area over the 19-year period for Black Crown Glacier. Overall, Adams Icefield has seen a decrease in the AAR between 1979 and 2019 which further suggests that this ice mass will continue to decrease in area and volume as time progresses due to a shrinking accumulation zone, and therefore increasing ablation zone.

Finally, we can also project the future fate of Baby Glacier by considering the total ice thickness and thinning rate. The maximum ice thickness remaining at Baby Glacier at both transects 00 and 01 is ~74 m. If we use the thickness change rate of -1.39 m year^{-1} and assume that it remains constant for the foreseeable future, then the ablation zone (Transect 00) of Baby Glacier will be lost by the year 2072. Similarly, if we use thickness change rate of -0.83 m year^{-1} for the mid-glacier transect (Transect 01) then Baby Glacier will be lost by the year 2108. Lastly, if we use the thickness change rate of -0.56 m year^{-1} for the accumulation zone transect (Transect 02) then Baby Glacier would disappear by the year 2115. In reality, complete losses might well occur before these dates as thinning rates tend to increase as ice masses become smaller (Serreze *et al.*, 2017). All three transects are located within the elevation range 850 m to 1100 m a.s.l. (Transect 00: ~900 m a.s.l.; Transect 01: ~980 m a.s.l.; Transect 02: ~1050 m a.s.l.) which is where 79.49% of Adams Icefield is situated, based on 2019 area measurements. As a result, these thickness changes can be extrapolated to the majority of Adams Icefield.

Due to the similarity in orientation, aspect, and size of Trent and Baby glaciers, and their close proximity, the thickness change rates from the ablation zone, mid-glacier, and accumulation zone of Baby Glacier can be applied to Trent Glacier, suggesting that Trent Glacier will disappear at a similar time that Baby Glacier does. However, the continued incising of Baby Glacier's accumulation zone from the main body of Adams Icefield and eventual detachment would result in Baby Glacier being the first ice mass to disappear completely from Adams Icefield. Although a newly studied concept within the glaciological community, the detachment of a glacier from a larger ice mass could potentially result in an accelerated retreat of the ice mass due to an increase in melt from the longwave radiation of the surrounding bedrock. Accelerated loss as a result of glacier detachment has been reported in the Clemenceau Icefield Group and Chaba Group, as well as the Columbia Icefield in Canadian Rockies (Jiskoot, *et al*., 2009; Rippin *et al*., 2020). The lack of incising at the saddle of Trent Glacier suggests that Baby Glacier will disappear first, followed by Trent Glacier based on size and aspect (south-facing). Black Crown Glacier will likely be the last ice mass to vanish due to its increased size (~0.5 km^2 larger than Trent and Baby glaciers) and aspect (north-facing). A north-facing aspect has a lower solar irradiance than a south facing aspect typically resulting in less substantial melt. Glacial ice at higher elevations will be the last to disappear, in the top part of Black Crown Glacier.

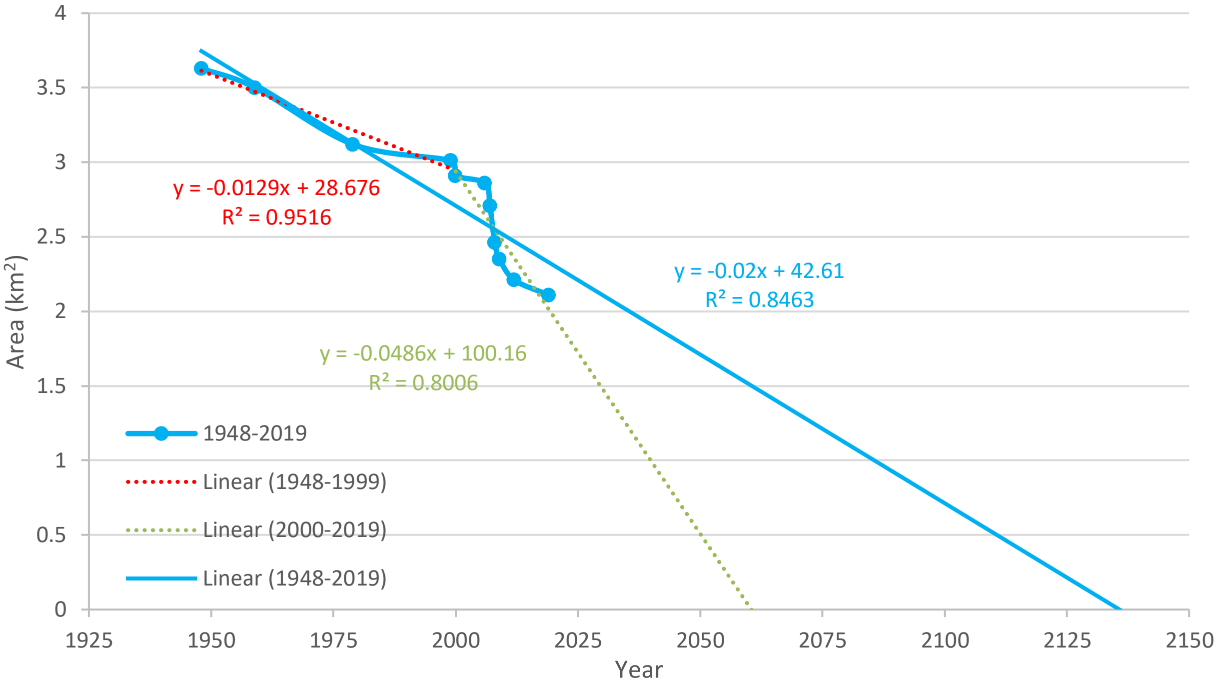

Figure 5.1. Historical area changes of Adams Icefield, and projected times of disappearance based on 1948-2019 area change (blue dotted line) and 2000-2019 area change (green dotted line).

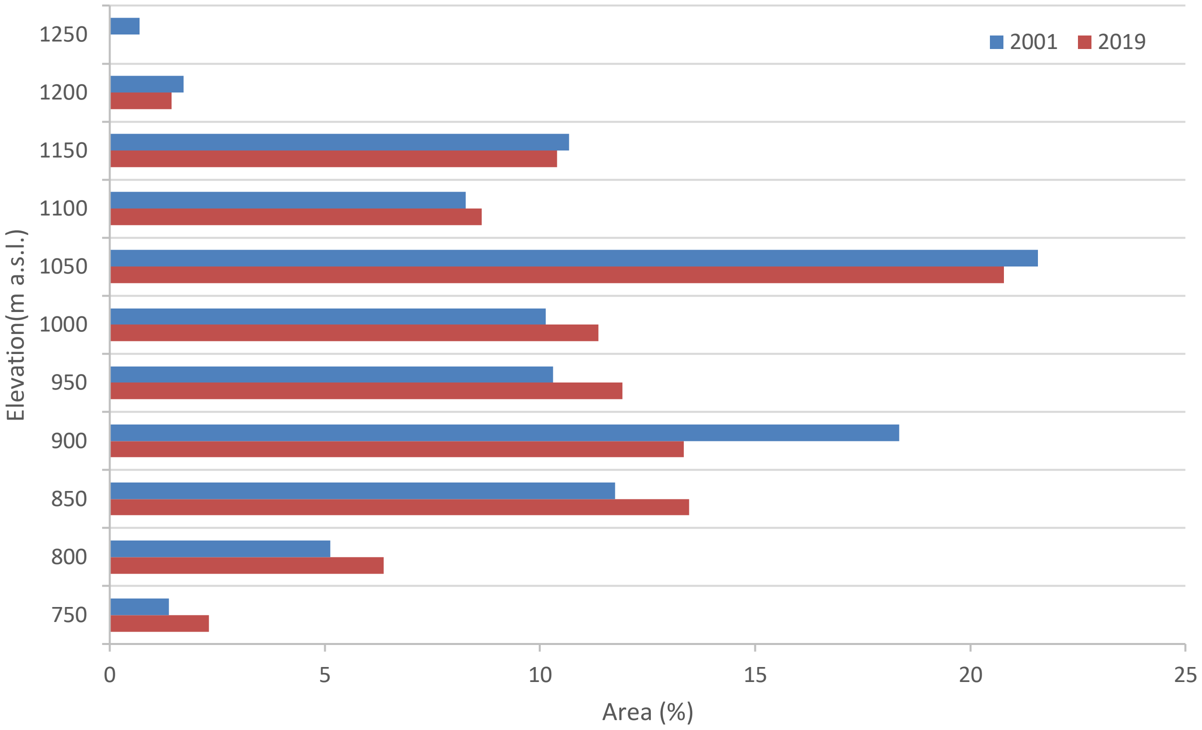

Figure 5.2. 2001 and 2019 hypsometry (50 m interval) of Adams Icefield.

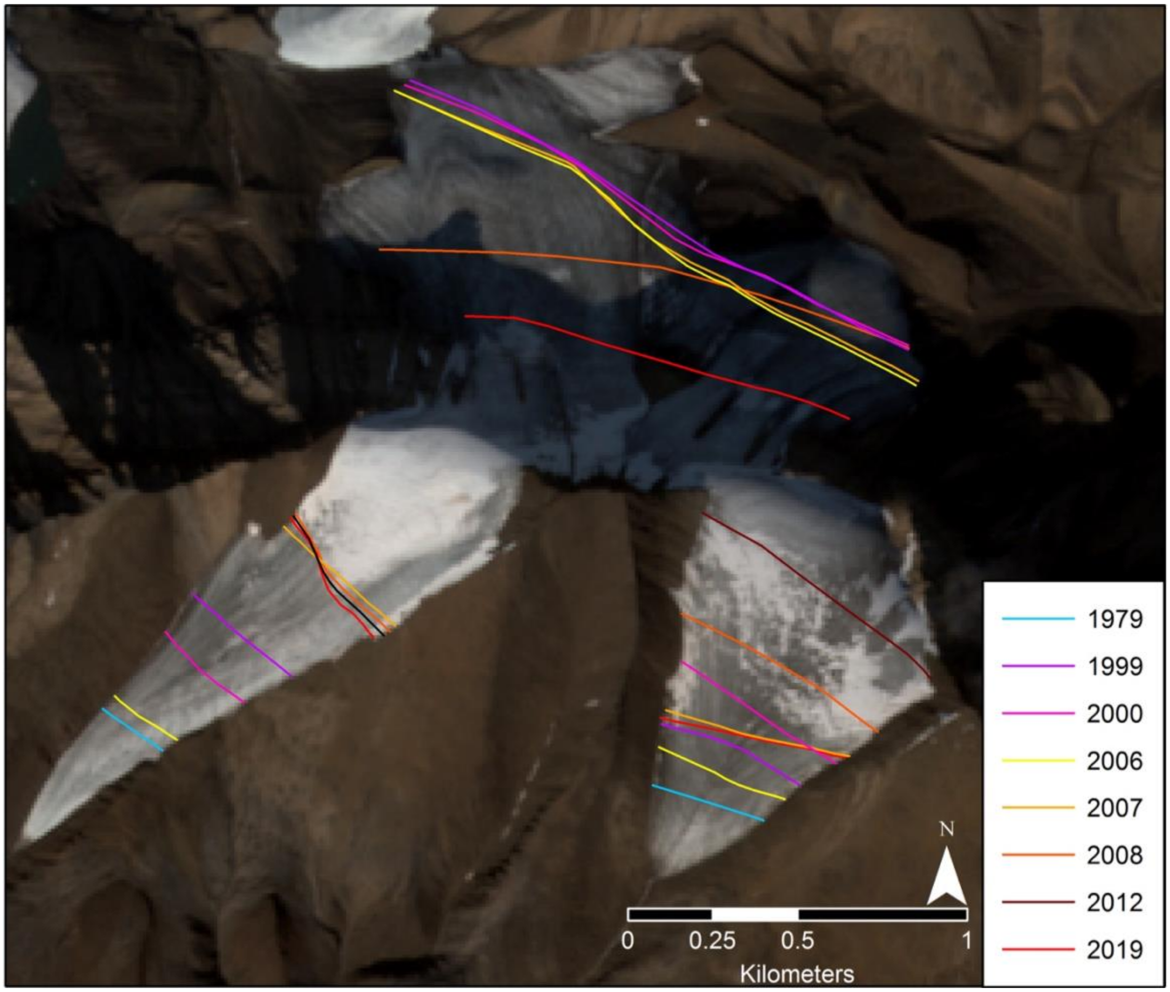

Figure 5.3. Changes in the elevation of the snow line of Adams Icefield between 1979 and 2019.

Table 5.1. Accumulation Area Ratio (AAR) of Baby, Trent, and Black Crown glaciers from 1979 to 2019.

Year	Baby Glacier AAR	Trent Glacier AAR	Black Crown Glacier AAR	Baby Glacier Snowline (m a.s.l.)
1979	0.92	0.90	-	894
2000	0.73	0.78	0.75	953
2012	0.28	0.55	-	1057
2019	0.74	0.57	0.44	1022

Chapter 6

CONCLUSION

This study presents the first comprehensive assessment of small glacier changes on Axel Heiberg Island, Nunavut, through the investigation of three separate objectives: Objective I examined the area changes of Adams Icefield and associated glaciers between 1948 and 2019; Objective II investigated volume and thickness changes of these ice masses between 1959 and 2019; and Objective III predicted the future fate of Adams Icefield using the results and analysis from objectives I and II.

Firstly, Objective I illustrated that Adams Icefield decreased in ice cover by 39.71% (total area loss: -1.52 km^2) over the 71-year period, with a mean area change rate of -0.0200 km^2 $year^{-1}$. A closer examination of the individual ice masses within Adams Icefield revealed that Trent Glacier lost the greatest amount of ice cover (-44%; total area loss: -0.37 km^2) between 1959 and 2019, followed by Black Crown Glacier (-40%; total area loss: -0.72 km^2) and Baby Glacier (-35%; total area loss: -0.29 km^2). Area change results from Adams Icefield are similar to those of other studies within the region. For example, White and Copland (2018) found that ice masses within the class size of 1-5 km^2 reduced in area by ~14% $decade^{-1}$ between 1999 and 2015 on Northern Ellesmere Island (Adams Icefield: -14.95% $decade^{-1}$).

Next, Objective II analyzed volume, mass, and thickness changes of Adams Icefield between 2001 and 2019. Findings from this analysis illustrated that Adams Icefield lost mass at a rate of -0.48 m w.e. $year^{-1}$ (total volume loss: -15.8 million m^3) between 2001 and 2012, and at a rate of -0.35 m w.e. $year^{-1}$ (total volume loss: -6.2 million m^3) between 2012 and 2019. Mass and volume loss was greatest at the termini of all three glaciers and decreased in rate as elevation was gained. As well, mass and volume was greatest at the margins of the icefield where the ice was in close proximity to exposed bedrock. Once again, results from this study are in close agreement to those from other studies such as Abdalati *et al*. (2004), who reported a loss of -0.5 m w.e. year^{-1} for ice masses within the QEI, such as Devon and Meighen ice caps, between 1995 and 2000.

Lastly, Objective III used the results from objectives I and II, as well as a thickness change analysis from a GPR survey, to predict when Adams Icefield will disappear entirely. Using the 1948-2019 area change rate (-0.0200 km^2 year^{-1}) Adams Icefield would lose its remaining 2.11 km^2 of ice cover by the 2130s, and by the 2060s if recent higher rates of area loss are used for the projections. A comparison between ice thicknesses across three transects on Baby Glacier and recent melt rates suggests that ice will completely disappear sometime between 2072 and 2115, depending on elevation.

Findings from this study illustrate that small (<1 km^2), low-lying ice masses such as Baby, Trent, and Black Crown glaciers are losing significant area and volume, particularly since the beginning of the twenty-first century. As a result, Adams Icefield will likely disappear entirely by the first decades of the twenty-second century, and perhaps well before that if current rates of warming continue.

References

Abdalatai, W., Krabill, W., Frederick, E., Manizade, S., Martin, S., Sonntag, J., Swift, R., Thomas, R., Yungel, J., Koerner, R. (2004). Elevation changes of ice caps in the Canadian Arctic Archipelago. *Journal of Geophysical Research*. 109.

Adams, W.P., Cogley, J.G., Ecclestone, M.A., Demuth, M.N. (1998). A small glacier as an index of regional mass balance: Baby Glacier, Axel Heiberg Island, 1959-1992. *Geografiska Annaler: Series A, Physical Geography*. 80(1), 37-50. DOI: 10.1111/j.0435-3676.1998.00025.

AMAP (2017). Snow, Water, Ice and Permafrost in the Arctic (SWIPA). Arctic Monitoring and Assessment Programme (AMAP). Oslo, Norway. Pg. 266.

Bader, H. (1954). Sorge's law of densification of snow on high polar glaciers. *Journal of Glaciology*. 2, 319-323.

Bahr, D.B., Radic, V. (2012). Significant contribution to total mass form very small glaciers. *Cryosphere*. 6, 763-770. DOI: 10.5194/tc-6-763-2012.

Berthier, E., Schiefer, E., Clarke, G. K. C., Menounos, B., and Remy, F. (2010). Contribution of Alaskan glaciers to sea-level rise derived from satellite imagery, Nat. Geosci., 3, 92–95, doi:10.1038/ngeo737.

Box, J.E., Coglan, W.T., Woutes, B., Burgess, D.O., O'Neel, S., Thomson, L.I., Mernild, S.H. (2018). Global sea-level contribution from Arctic land ice: 1971-2017. *Environ. Res. Lett*. 13, pg. 1-12. DOI: 10.1088/1748-9326/aaf2ed.

Braithwaite, R.J. (2019). Geography of Glacier Mass Balance. Thesis submitted to the University of Manchester. Pg. 221.

Braun, C., Hardy, D.R., Bradley, R.S. (2004). Mass balance and area changes of four High Arctic plateau ice caps, 1959-2002. *Geogr. Ann*. 86(1), 43-52.

Canada's Changing Climate Report (CCCR). (2019). *Changes in snow, ice, and permafrost across Canada*. Retrieved from https://changingclimate.ca/site/assets/uploads/sites/2/2018/11/CCCR_Chapter5-Changes-in-Snow-Ice-and-Permafrost-Across-Canada.pdf

Cazenave, A. and 88 others (2018). Global sea-level budget 1993-present. *Earth Syst. Sci. Data*. 10, 1551-1590.

Cogley, J.G., Adams, W.P. (2000). Remote-sensing resources for monitoring glacier fluctuations on Axel Heiberg Island. *Arctic*. 53(3), 258-259.

Cogley, J.G., Adams, W.P., Ecclestone, M.A. (2011). Half a Century of Measurements of Glaciers on Axel Heiberg Island, Nunavut, Canada. *Arctic*. 64(3), 371-375.

Cohen, J., Screen, J. A., Furtado, J. C., Barlow, M., Whittleston, D., Coumou, D., Francis, J., Dethloff, K., Entekhabi, D., Overland, J. and Jones, J. (2014) Recent Arctic amplification and extreme mid-latitude weather. *Nature Geoscience,* 7, 627-637.

Copland, L. and Sharp, M. (2001). Mapping thermal and hydrological conditions beneath a polythermal glacier with radio-echo sounding. *Journal of Glaciology,* 47(157), 232-242

Copland, L., Sharp, M., Dowdeswell, J. (2003). The distribution and flow characteristics of surge-type glaciers in the Canadian High Arctic. *Annals of Glaciology*. 36, 73-81.

Farinotti, D., Huss, M., Furst, J.J., Landmann, J., Machguth, H., Maussion, F., Pandit, A. (2019). A consensus estimate for the ice thickness distribution of all glaciers on Earth. *Nature Geoscience*. 12, 168-173.

Flanner, M.G., Zender, C.S., Randerson, T.J., Rasch, P.J. (2007). Present-day climate forcing and response from black carbon in snow. *J. Geophys. Res*. 112.

Gardner, A.S., Moholdt, G., Wouters, B., Wolkjen, G.J., Burgess, D.O., Sharp, M.J., Cogley, J.G., Braun, C., Labine, C. (2011). Sharply increased mass loss from glaciers and ice caps in the Canadian Arctic Archipelago. *Nature*. DOI: 10.1038/nature10089.

Girod, L., Nuth, C., Kaab, A., McNabb, R., Galland, O. (2017). MMASTER: Improved ASTER DEMs for Elevation Change Monitoring. *Remote Sensing*. 9(7), 704. DOI: 10.3390/rs9070704.

Hagen, J.O., Melvold, K., Pinglot, F., Dowdeswell, J. (2003). On the net mass balance of the glaciers and ice caps in Svalbard, Norwegian Arctic. *Arctic, Antarctic, and Alpine Research*. 35(2), 264-270.

Hall, D.K., Baa, K.J., Bindschadler, R.A., Chein, J.Y.L. (2003). Consideration of the errors inherent in mapping historical glacier positions in Austria from the ground and space (1893-2001). *Remote Sensing of the Environment*. 86, 566-577.

Huss, M. (2013). Density assumptions for converting geodetic glacier volume change to mass change. *The Cryosphere*. 7, 877-887.

Huss, M., Fisher, M. (2016). Sensitivity of very small glaciers in the Swiss Alps to future climate change. *Frontiers in Earth Sciences*. 4(34). DOI: 10.3389/feart.2016.00034.

Huss, M., Hock, R. (2015). A new model for global glacier change and sea-level rise. *Frontiers in Earth Sciences*. 3:54. DOI: 10.3389/feart.2015.00054.

Jiskoot, H., Curran, C.J., Tessler, D.L., Shenton, L.R. (2009). Changes in Clemenceau Icefield and

Chaba Group glaciers, Canada, related to hypsometry, tributary detachment, length-slope and area-aspect relations. *Annals of Glaciology*. 50(53), 133-143.

Koerner, R.M. (2005). Mass balance of glaciers in the Queen Elizabeth Islands. Nunavut, Canada. *Annals of Glaciology*. 42, 417-423.

Lenaerts, J., van Angelen, J., van den Broeke, M., Gardner, A., Wouters, B., van Meijgaard, E. (2013). Irreversible mass loss of Canadian Arctic Archipelago glaciers. *Geophys. Res. Lett*. 40, 870-874. DOI: 10.1002/grl.50214.

Lesins, G., Duck, T.J., Drummond, J.R. (2010). Climate trends at Eureka in the Canadian High Arctic. *Atmosphere-Ocean*. 48(2), 59-80.

Maksym, T. (2019). Arctic and Antarctic Sea Ice Change: Contrasts, Commonalities, and Causes. *Annual Review of Marine Science*. 11, 187-213.

Medrzycka, D., Copland, L., Van Wychen, W., Burgess, D. (2019). Seven decades of uninterrupted advance of Good Friday Glacier, Axel Heiberg Island, Arctic Canada. *Journal of Glaciology*. 65(251), 440-452. DOI: 10.1017/jog.2019.21.

Millan, R., Mouginot, J., Rignot, E. (2017). Mass budget of the glaciers and ice caps of the Queen Elizabeth Islands, Canada, from 1991 to 2015. *Environ. Res. Lett*. 12, pg. 1-12.

Moon, T., Ahlstrom, A., Goelzer, H., Lipscomb, W., Nowicki, S. (2018). Rising Oceans Guaranteed: Arctic Land Ice Loss and Sea Level Rise. *Curr. Clim. Change Rep*. 4, 211-222.

Morin, P., Porter, C., Cloutier, M., Howart, I., Noh, M.J., Willis, M., Bates, B., Williamson, C., Peterman, K. (2016). ArcticDEM; A Publically Available, High Resolution Elevation Model of the Arctic.

Mortimer, C.A., Sharp, M., Wouters, B. (2016). Glacier surface temperatures in the Canadian High Arctic, 2000-15. *Journal of Glaciology*. 62(325), 963-975.

Mortimer, C.A. (2017). *Ice surface temperature, albedo, and surface elevation change of glaciers and ice caps of the Queen Elizabeth Islands, Nunavut, Canada, 1995-2015*. Doctoral dissertation (University of Alberta, Edmonton, Canada). Retrieved from https://era.library.ualberta.ca/items/45d0a907-3384-4ad3-aa3e-8f71e616142f/view/e6008ab8-424c-498e-97f1-dd64e86781da/MortimerCA_PhD_thesis_April2017.pdf

Mortimer, C.A., Sharp, M. (2018). Spatiotemporal variability of Canadian High Arctic glacier surface albedo from MODIS data, 2001-2016. *The Cryosphere*. 12, 701-720.

Mortimer, C.A., Sharp, M., Van Wychen, W. (2018). Influence of recent warming and ice dynamics on glacier surface elevations in the Canadian High Arctic, 1995-2014. *Journal of Glaciology*. 64(245), 450-464.

Noel, B., van de Berg, W.J., Lhermitte, S., Wouters, B., Schaffer, N., van den Broeke, M.R. (2018). Six decades of glacial mass loss in the Canadian Arctic Archipelago. *Journal of Geophysical Research: Earth Surface*. 123, 1430-1449.

Ommanney, C.S.L. (1969). A study in glacier inventory: the ice masses of Axel Heiberg Island, Canadian Arctic Archipelago. *Axel Heiberg Island Research Reports Glaciology 3*.

Paul, F., Haeberli, W. (2008). Spatial variability of glacier elevation changes in the Swiss Alps obtained from two digital elevation models. *Geophysical Research Letters*. 35.

Pfeffer, W.T., Arendt, A.A., Bliss, A., Bolch, T., Cogley, J.G., Gardner, A.S., Hagen, J.O., Hock, R., Kaser, G., Kienholz, C., Miles, E.S., Moholdt, G., Molg, N., Paul, F., Radic, V., Rastner, P., Raup, B.H., Rich, J., Sharp, M.J., The Randolph Consortium. (2014). The Randolph Glacier Inventory: a globally complete inventory of glaciers. *Journal of Glaciology*. 60(221), 537-552. DOI: 10.3189/2014JoG13J176.

Rippin, D.M., Sharp, M., Van Wychen, W., Zubot, D. (2020). 'Detachment' of icefield outlet glaciers: catastrophic thinning and retreat of the Columbia Glacier (Canada). *Earth Surface Processes and Landforms*. 45, 459-472.

RGI Consortium (2017). Randolph Glacier Inventory – A Dataset of Global Glacier Outlines: Version 6.0: Technical Report, Global Land Ice Measurements from Space, Colorado, USA. Digital Media. DOI: https://doi.org/10.7265/N5-RGI-60

Serreze, M.C., Raup, B., Braun, C., Hardy, D.R., Bradley, R.S. (2017). Rapid wastage of the Hazen Plateau ice caps, northeastern Ellesmere Island, Nunavut, Canada. *The Cryosphere*. 11, 169-177.

Sharp, M., Burgess, D.O., Cogley, J.G., Ecclestone, M., Labine, C., Wolken, G.J. (2011). Extreme melt on Canada's Arctic ice caps in the 21st century. *Geophys. Res. Lett*. 38, 1-5. DOI: 1029/2011GL047381.

Sharp, M., Burgess, D.O., Cawkwell, F., Copland, L., Davis, J.A., Dowdeswell, E.K., Dowdeswell, J.A., Gardner, A.S., Mair, D., Wang, L., Williamson, S.N., Wolken, G.J., Wyatt, F. (2014). Remote sensing of recent glacier changes in the Canadian Arctic. *Global Land Ice Measurements from Space*. 9, 205-228.

Sharp, M., Wolken, G., Burgess, D., Cogley, J.G., Copland, L., Thomson, L., Arendt, A., Wouters, B., Kohler, J., Andreassen, L.M., O'Neel, S., Pelto, M. (2015). Glaciers and ice caps outside Greenland [in State of the Climate in 2014]. *Bull. Am. Meterol. Soc*. 96(7), 135-137.

Stroeve, J., Barrett, A., Serreze, M., Schweiger, A. (2014). Using records from submarine, aircraft and satellites to evaluate climate model simulations of Arctic sea ice thickness. *The Cryosphere*. 8, 1839-1854.

Thomson, L.I., Osinski, G.R., Ommanney, S.L. (2011). Glacier change on Axel Heiberg Island, Nunavut, Canada. *Journal of Glaciology*. 57(206), 1079-1086.

Thomson, L.I., Copland, L. (2016). White Glacier 2014, Axel Heiberg Island, Nunavut: mapped using Structure from Motion methods. *Journal of Maps*. 12(5), 1063-1071. DOI: 10.1081/17445647.2015.1124057.

Thomson, L.I., Zemp, M., Copland, L., Cogley, G., Ecclestone, M. (2017). Comparison of geodetic and glaciological mass budgets for White Glacier, Axel Heiberg Island, Canada. *Journal of Glaciology*. 63(237), 55-66. DOI: 10.1017/jog.2016.112.

Van Wychen, W., Burgess, D.O., Gray, L., Copland, L., Dowdeswell, J.A., Benham, T.J., (2014). Glacier velocities and dynamic ice discharge from the Queen Elizabeth Islands, Nunavut, Canada. *Geophys. Res. Lett*. 41(2), 484-490.

Van Wychen, W., Copland, L., Burgess, D., Gray, L. and Schaffer, N. (2015): Glacier velocities and dynamic discharge from the ice masses of Baffin Island and Bylot Island, Nunavut, Canada. *Canadian Journal of Earth Sciences*. 52(11), 980-989.

Van Wychen, W., Davis, J., Burgess, D.O., Copland, L., Gray, L., Sharp, M., Mortimer, C. (2016). Characterizing interannual variability of glacier dynamics and dynamic discharge (1999-2015) for the ice masses of Ellesmere and Axel Heiberg Islands, Nunavut, Canada. *Journal of Geophys. Res. Earth Surface*. 121(1), 39-63.

Walsh, J.E. (2014). Intensified warming of the Arctic: Causes and impacts on middle latitudes. *Global and Planetary Change*. 117, 52-63.

White, A., Copland, L. (2018). Area change of glaciers across Northern Ellesmere Island, Nunavut, between ~1999 and ~2015. *Journal of Glaciology*. 6(246), 609-623.

Williams, R.S., Hall, D.K., Sigurdsson, O., Chien, J.Y.L. (1997). Comparison of satellite-derived with ground-based measurements of the fluctuations of the margins of Vatnajokull, Iceland, 1973-92. *Annals of Glaciology*. 24, 72-80.

Wolf, P.R., Dewitt, B.A. (2000). *Elements of Photogrammetry, with Applications in GIS*. Third Edition. McGraw-Hill, New York. 608 pages.

Wolken, G., Sharp, M.J., Andreassen, L.M., Burgess, D.O., Copland, L., Kohler, J., O'Neel, S., Pelto, M.S., Thomson, L.I., Wouters, B. (2017). State of the Climate in 2016. *Bull. Am. Meteor. Soc*. 98.

Wouters, B., Gardner, A.S., Moholdt, G. (2019). Global glacier mass loss during the

GRACE satellite mission (2002-2016). *Frontiers in Earth Science*. 7:96.